SANDIA REPORT
SAND2018-10541
Unlimited Release
Printed September, 2018

Innovative Technologies for Optical Detection of Stress Corrosion Cracks

Charles R. Bryan, Kent B. Pfeifer, Stephen Buerger, and Eric J. Schindelholz

Prepared by
Sandia National Laboratories
Albuquerque, New Mexico 87185 and Livermore, California 94550

Sandia National Laboratories is a multimission laboratory managed and operated by National Technology and Engineering Solutions of Sandia, LLC, a wholly owned subsidiary of Honeywell International, Inc., for the U.S. Department of Energy's National Nuclear Security Administration under contract DE-NA0003525.

Issued by Sandia National Laboratories, operated for the United States Department of Energy by National Technology and Engineering Solutions of Sandia, LLC.

Available to DOE and DOE contractors from

U.S. Department of Energy
Office of Scientific and Technical Information
P.O. Box 62
Oak Ridge, TN 37831

Telephone: (865) 576-8401
Facsimile: (865) 576-5728
E-Mail: reports@osti.gov
Online ordering: http://www.osti.gov/scitech

Available to the public from

U.S. Department of Commerce
National Technical Information Service
5301 Shawnee Rd
Alexandria, VA 22312

Telephone: (800) 553-6847
Facsimile: (703) 605-6900
E-Mail: orders@ntis.gov
Online order: https://classic.ntis.gov/help/order-methods/

SAND2018-
10541105411054110541105411054110541105411054110541105411054110541105411054110541105
41105411054110541105411054110541105411054110541105411054110541105411054110541105411
05411054110541105411054110541105411054110541105411054110541105411054110541105411054
11054110541105411054110541105411054110541105411054110541105411054110541105411054110
54110541105411054110541105411054110541105411054110541105411054110541105411054110541
10541105411054110541105411054110541105411054110541105411054110541105411054110541105
41105411054110541105411054110541105411054110541105411054110541105411054110541105411
05411054110541105411054110541105411054110541105411054110541105411054110541105411054
11054110541105411054110541105411054110541105411054110541105411054110541105411054110
54110541105411054110541105411054110541105411054110541105411054110541
Printed September 2018
Unlimited Release

Innovative Technologies for Optical Detection of Stress Corrosion Cracks

Charles R. Bryan
Department 8845, Storage and Transportation Technologies

Kent B. Pfeifer
Department 8634, Nano and Microsensors

Stephen Buerger,
Department 6533, Robotics and Counter Robotics R&D

Eric J. Schindelholz
Department 1852, Materials Reliability

Sandia National Laboratories
P. O. Box 5800
Albuquerque, New Mexico 87185

Abstract

Stress corrosion cracks (SCC) represent a major concern for the structural integrity of engineered metal structures. In hazardous or restricted-access environments, remote detection of corrosion or SCC frequently relies on visual methods; however, with standard VT-1 visual inspection techniques, probabilities of SCC detection are low. Here, we develop and evaluate an improved optical sensor for SCC in restricted access-environments by combining a robotically controlled camera/fiber-optic based probe with software-based super-resolution imaging (SRI) techniques to increase image quality and detection of SCC. SRI techniques combine multiple images taken

at different viewing angles, locations, or rotations, to produce a single higher-resolution composite image. We have created and tested an imaging system and algorithms for combining optimized, controlled camera movements and super-resolution imaging, improving SCC detection probabilities, and potentially revolutionizing techniques for remote visual inspections of any type.

ACKNOWLEDGMENTS

The authors would like to thank team members Clinton Hobart (6532), Mike Martinez (65330, Sean Hendrix (6531), and Art Rumpf (8634) for their contributions to the project. We are indebted to GE Inspection Technologies for the loan of the GE Videoprobe, and to Robotic Technologies of Tennessee for their technical advice on integrating our system with their robotic vehicle.

TABLE OF CONTENTS

FIGURES

TABLES

EXECUTIVE SUMMARY

Stress corrosion cracks represent a major concern for the structural integrity of engineered metal structures, and standard visual techniques for detecting stress corrosion cracks (SCC), are ineffective. Here, we have created and tested an improved optical sensor for SCC in restricted access-environments by combining optimized, controlled camera movements and super-resolution image (SRI) processing. SRI processing combines multiple images of a subject to create a final image that is higher resolution than any of the individual images used to create it. Our approach is innovative in that we utilize a priori knowledge of the camera location for each individual image to align, or register, the images with each other, resulting in a superior SRI final image relative to techniques using software registration.

To evaluate this approach, benchtop testing was performed with three different cameras: a laboratory digital microscope, a coarsely pixelated coherent fiber optic borescope, and a high resolution CCD-based borescope used in industry visual inspections. High-precision X-Y and rotational stages were used to image laboratory-created test samples with real SCC cracks in these tests. Testing indicated that SRI processing improved crack imaging with all imaging devices. Moreover, testing indicated that pre-processing to remove lens distortion was effective in improving final images; for the fiber optic borescope, additional pre-processing with a fast Fourier transform filter to remove coarse optical fiber pixelation was also useful. Testing also showed that final image quality improved with the number of images combined. Finally, the benchtop tests confirmed that using *a priori* knowledge of the camera location for each individual image resulted in a higher quality combined image.

Having confirmed the benefit of using the camera location to register the individual images, we designed and built a high-precision module for controlling camera motions. This system was built for the specific application of inspecting spent nuclear fuel storage canisters within their overpacks. Access to the canisters is limited by narrow ventilation channels through the overpacks and narrow annuli between the overpack and the canister surface. Moreover, high radiation levels and potentially elevated temperatures can be present. Rather than developing a robot to enter the overpack, the module was designed to be coupled to an existing robotic delivery system designed by Robotic Technologies of Tennessee. This magnetic-wheeled robot is capable of entering the overpack and the annulus by traveling on the carbon steel wall of the overpack. The system also incorporated a high-resolution videoprobe borrowed from GE Inspection Technologies, that has been used in several canister inspections to date.

A wood and steel mockup of a NAC International SNF storage system was built to test the combined robot/camera module system, including the steel-lined ventilation channel through the overpack, and a portion of the annulus between the canister and the overpack. The combined robot/imager system successfully navigated the tight ventilation channel and entered the annulus, positioning itself to inspect the canister surface. This demonstrates that the system could be used in a real storage system.

This work serves as a successful proof-of-concept, demonstrating that an appropriate imaging system can be delivered through the available access channel to the surface of a NAC canister mockup, and that such an imaging system may be used with SR imaging techniques to locate extremely small stress corrosion cracks. All of the key system elements have been demonstrated independently or as subsystems, but a complete end-to-end experiment has not yet been

conducted. To mature the system to a level suitable for field use requires several additional steps, including software development for controlling the motion module and for integration with the imager; re-engineering packaging and cabling for the robot/image system to improve cable management and robustness; and software automation for real-time SRI processing and analysis. With additional effort the imaging system built here could be the basis for a robust SCC crack detection system for deployment in spent nuclear fuel storage systems.

NOMENCLATURE

Abbreviation	Definition
ASME	American Society of Mechanical Engineers
CCD	charge coupled device
DOE	Department of Energy
EPRI	Electric Power Research Institute
FFT	fast Fourier transform
GE	General Electric
IRP	[DOE] Integrated Research Program
ISFSI	independent spent fuel storage facility
NDE	non-destructive evaluation
NEUP	[DOE] Nuclear Energy University Programs
NRC	Nuclear Regulatory Commission
NWTRB	Nuclear Waste Technical Review Board
RTT	Robotic Technologies of Tennessee
SCC	stress corrosion cracking
SNF	spent nuclear fuel
SNR	signal-to-noise ratio
SRI	super-resolution imaging

1. INTRODUCTION

Many non-destructive evaluation (NDE) techniques exist for detection of stress corrosion cracks (SCC) in metal structures. However, many ultrasound- or eddy current-based NDE methods are difficult or impossible to perform remotely or in restricted-access environments, so remote detection of corrosion or SCC frequently relies on visual methods, using camera or coherent fiber optic imaging tools. VT-1 inspections require equipment capable of resolving 1.1 mm text, but SCC widths are commonly in the 16-30-micron range [1], more than 30 times smaller than the text used in VT-1 resolution tests, and probabilities of SCC detection using visual methods are low [2]. High-resolution cameras can improve resolution, but are susceptible to radiation damage and cannot be used in high-radiation environments. Typical radiation-hardened cameras have low resolution (640x480 pixels), and fiber optic-based imaging systems are even lower-resolution. Here, we have developed an improved optical sensor for SCC in restricted access-environments by combining a camera/fiber-optic based probe with software-based super-resolution imaging (SRI) techniques to increase image quality and detection of SCC. SRI techniques combine multiple images taken at different viewing angles, locations, or rotations, to produce a single composite image with up to a factor of 10 improvement in resolution relative to the original images [3, 4].

SRI processing techniques have been used for many years, first showing up in the 1990s, but receiving expanded attention in the 2000s [4, 5]. In scientific applications, they have only been widely used for fluorescence microscopy, allowing imaging of features well below the diffraction limit for the wavelength of light used [6, 7]. The techniques are well developed for microscopy applications, and are being increasing utilized in other imaging applications; development of SRI algorithms continues at a rapid pace [e.g., 8, 9, 10]. However, no optimization of camera motions or angles is used, although some microscope systems do use camera arrays to take multiple images simultaneously for SRI processing. Use of SRI techniques for improving SCC detection has been proposed previously [3], but only reprocessed still images captured from video records of inspections. Here, we have built a prototype that precisely moves the imaging device while capturing multiple images. By taking full advantage of the known translations in viewing angle and position, we have developed and optimized SRI processing techniques to yield the highest possible final image quality, maximizing feature resolution and the likelihood of detecting SCC. The concept of deliberately optimizing camera translations and imaging angles in real-time to get the optimal final composite image is unique.

Creating an imaging system and algorithms for combining optimized, controlled camera movements and super-resolution imaging holds potential for greatly improving SCC detection probabilities, as well as potentially revolutionizing techniques for remote visual inspections of any type. While potentially of broad application, immediate needs for such a tool include detection of SCC in nuclear reactor vessels and piping, and detection of SCC in spent nuclear fuel (SNF) dry storage canisters within their overpacks. Other potential applications include inspection of occluded

areas in aircraft frames, that currently require costly disassembly to access for inspection. To limit this project to a manageable scope, we have developed our

system to specifically address SNF dry storage canister inspections. With that application in mind, we have developed our system to fit within the restricted spaces of SNF storage system overpacks, and have combined it with a robotic delivery system that has previously been successfully used to enter the overpacks. We have tested three different imaging tools, including the same video imaging system that been used in all in-field canister inspections to date, a General Electric (GE) Inspection Technologies XLG3 Videoprobe.

In Section 2 of this report, an overview of SNF interim storage systems is given, and the requirements for the imaging system are discussed. In Section 3, the basics of super-resolution image processing are explained, and the approach to implementing it for this project is described. In Section 4, benchtop experiments used to develop and test different SRI imaging techniques are described. Three different imaging tools—a digital camera, a coherent fiber optic cable, and the GE video camera used in SNF storage canister inspections—were tested, and examples and results for each device are provided. In Section 4, the development of the robotic "motion stage" and integration with the robotic delivery system (obtained from an external vendor) is described. In Section 5, integration and testing of the imaging system with the delivery system is discussed. Finally, results and recommendations for further work are given in Section 6.

2. INSPECTION OF SNF DRY STORAGE CANISTERS

In the U.S., there are currently 99 operating commercial nuclear reactors at 61 sites. Including decommissioned reactors and other storage sites, there are over 80,000 metric tons of spent nuclear fuel (SNF) in storage at about 70 different Independent Spent Fuel Storage Installations (ISFSIs) (Figure 1). Initially, SNF is removed from the reactor core and stored in cooling pools. Over time, SNF radiation levels decrease and heat output drops. Following initial cooling in pools, the SNF is transferred to dry storage systems for longer-term storage at the reactor sites. Currently, about 30% of existing SNF is stored in a total of about 2700 storage systems. The dry storage systems are intended as interim storage until a permanent disposal site is developed, and until recently, were licensed for up to 20 years, with the potential for renewals also up to 20 years. In 2011, 10 CFR 72.42(a) was modified to allow for initial license periods of up to 40 years, with the possibility of license extensions of an additional 40 years. Under all foreseeable scenarios, some SNF will remain in dry storage for much longer than the original design specifications for the storage systems. The potential for corrosion of the storage canisters during this extended period is a subject of ongoing investigation by the U.S. Nuclear Regulatory Commission (NRC), industry, and the U.S. Department of Energy (DOE).

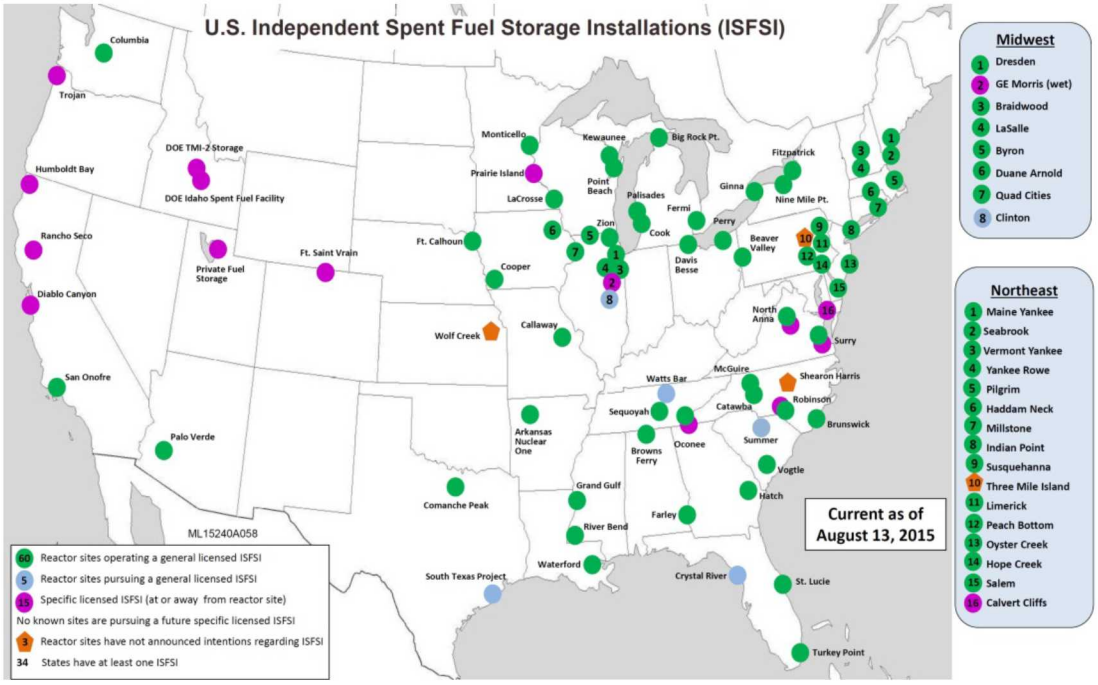

Figure 1: U.S. Independent Spent Fuel Storage Installations
http://www.nrc.gov/waste/spent-fuel-storage.html. downloaded 8/26/2016

Typically, the storage systems are welded stainless steel containers enclosed in passively ventilated concrete, or steel and concrete, overpacks (Hanson et al., 2012). For most dry cask storage systems, passive ventilation is used to cool the casks within the overpacks, and large volumes of outside air are drawn through the system by natural convection. Figure 2 illustrates the standard vertical and horizontal canistered dry storage systems that are most common in the U.S. fleet. The passive cooling

Vertical—In vertical systems, the welded stainless steel canister sits upright within a steel-lined concrete overpack. The canister is passively cooled by air that enters through inlets at the bottom of the overpack and exits through vents near the top.

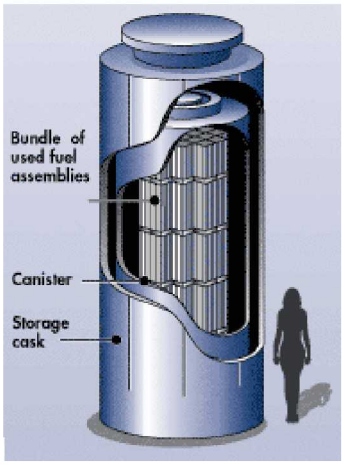

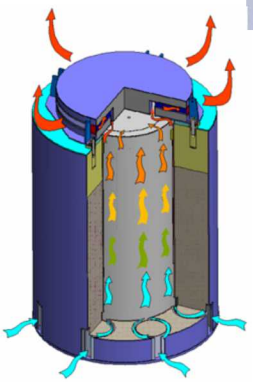

Pathway for air flow through the overpack.

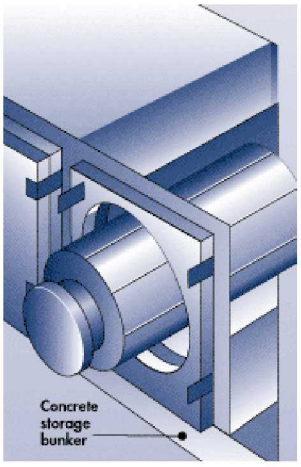

Horizontal—In horizontal systems, the welded canister rests on its side upon rails within a concrete vault. Air enters the overpack through a vent in the base, flows up and around the canister, and exits through vents on the roof.

Figure 2. Canistered Dry Storage Systems—Two Basic Designs.

function is also illustrated. The principal reason for the cooling is to maintain thermal limits established by the NRC for the fuel cladding.

Inherent in this passive design is the potential for dust and aerosols within the air to be deposited on the steel canisters, and, as the casks cool over time, salts in the dust will deliquesce (absorb water) to form brine on the storage container surface. If the salts contain aggressive components such as chloride, localized attack can occur. Most modes of corrosion, including general corrosion, pitting, and crevice corrosion, cannot significantly damage the steel canisters within anticipated storage times. However, one corrosion mechanism, chloride-induced SCC, may propagate relatively rapidly under some conditions and could potentially result in canister penetration during long-term interim storage. Chloride-induced SCC is a well-documented mode of attack for stainless steels (including 304SS and 316SS) in marine environments [11], and many ISFSIs are located in coastal areas.

Because of the longer-than-intended storage times and the potential for a corrosive environment, SCC of interim storage containers has been determined to be a high priority data gap by the Nuclear Waste Technical Review Board [12], the Electric Power Research Institute [13], the DOE [14], and the NRC [15]. Several DOE-funded institutions and industry groups are currently evaluating the potential for SCC occurrence and penetration of SNF interim storage canisters, and are working to develop techniques and procedures to inspect canisters for SCC. DOE has funded work at national laboratories including Sandia, Savannah River, and Pacific Northwest National Laboratories; by several different universities through the Nuclear Energy University Program (NEUP) and Integrated Research Program (IRP) projects; and by small businesses through Small Business Innovation Research (SBIR) projects. EPRI has worked with volunteer industry partners and DOE labs to evaluate the composition of deposits on the surface of in-service interim storage canisters, and now is working with industry to develop techniques to inspect storage canisters within their overpacks for SCC. EPRI is testing robotic delivery systems for entering overpacks, and has tested eddy current and ultrasound sensors with little success. They are focusing on visual systems now, but acknowledge that it is uncertain if detection of SCC using standard VT-1 methods will be possible. Storage system vendors are also working to develop inspection tools. Finally, at the request of the NRC, the American Society of Mechanical Engineers (ASME) is developing a formal standard procedure for performing canister inspections using visual methods, but recognizes that available VT-1 methods may be ineffective. There is a strong need for an improved visual inspection method. This project will demonstrate the usefulness of using SRI processing to improve SCC detection, and stimulate further work in this area.

The initial storage system licensing periods are approaching expiration at many sites, and those sites are preparing for canister inspections, as required for recertification. There is an immediate need for technology capable of detecting stress corrosion cracks on in-service spent nuclear storage canisters within their overpacks. This would require a device able to withstand high temperatures and radiation levels while fitting into the narrow gap between the canister and overpack. There is presently no solution to detect such cracks, creating a significant risk as the storage canisters age.

The need for a technical solution for *in situ* evaluation of canister surfaces is growing. Challenges for these inspections include the high temperatures and high radiation levels at the canister surfaces (1,000-10,000 rem/hr) which force the use of remote inspection techniques, and difficulties in accessing the canister surface within the overpack. For *in situ* evaluation, entry into the overpack must occur through ventilation channels, which commonly have small openings. Moreover, to avoid radiation shine, the ventilation channels never offer line-of-sight access to the canister, frequently containing right-angle steps to prevent any radiation shine from escaping the overpack. However, access through the vents is not impossible; the vents have been used for access during several EPRI-led efforts to sample dusts on the canister surfaces over the past several years (Figure 3). Once inside the overpack, access is limited by narrow annuli between the canister walls and the overpack.

An additional complexity is the variability in storage system designs. Two of the three major storage system vendors, HOLTEC International and NAC International, make vertical systems (Figure 2), while the third, Areva-TN, makes horizontal systems. HOLTEC systems have a smaller annulus (nominally, 2 inches) between the canister and the overpack than the NAC systems (nominal 4 inch annulus). The crypt-like horizontal systems contain no annulus *per se*, and spaces within the overpack are much larger. Moreover, each manufacturer has built many models over the years; in all, over 30 different storage system designs have been licensed.

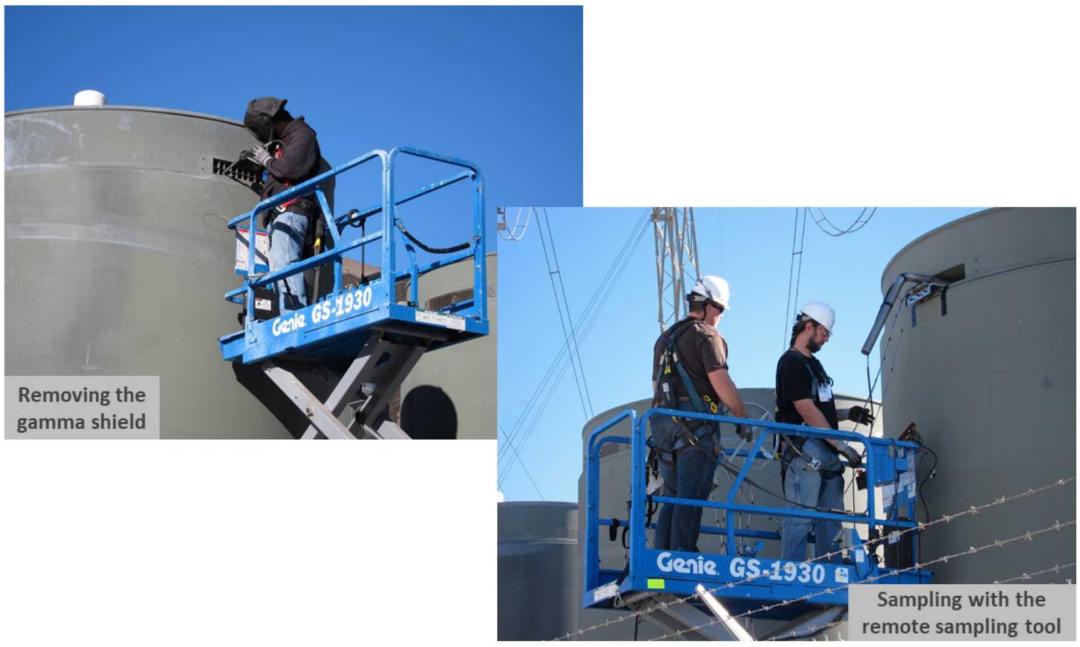

Figure 3. Entering the ventilation openings to sample dusts on the surface of SNF dry storage canisters within their overpacks.

The goal of this project is to demonstrate the effectiveness of combining SRI processing with controlled camera motions to improve SCC detection, with the final goal of building a prototype device to demonstrate the utility of the method. To keep the scope of this study to a manageable size, we have concentrated on a single storage system design, based on the NAC storage systems. This system was chosen because significant progress has been made in building robots able to move through the annulus and inspect canisters in the NAC systems. Specifically, EPRI has worked with Robotic Technologies of Tennessee (RTT) to design robots that can enter the ventilation openings in the NAC systems and move down the annulus between the overpack and the canister. The robots have magnetic wheels, and move down the carbon steel overpack walls, deploying tools against the canister surface. One such robot is shown in Figure 4. As described in Section 5, we have purchased one of the RTT robots and used it as a delivery system for our camera module. We have also made a wood and steel mockup of a typical ventilation channel in a NAC system, to test insertion of the delivery system and imaging module. Here, we demonstrate that combining SRI processing with controlled camera movements can be built on a scale sufficiently small to enter SNF dry storage systems and can be effectively utilized to inspect SNF storage canisters within their overpacks.

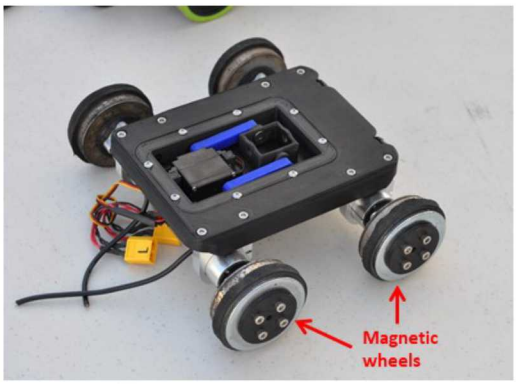

Magnetic Robot
(Robotic Technologies of Tennessee)

Testing a magnetic robot on a storage system cutaway, Palo Verde Nuclear Plant Education Center

Figure 4. Magnetic Robot for Use with NAC Vertical Storage Systems.

3. PRINCIPLES OF SUPER RESOLUTION IMAGING

3.1. Basic concept

The acquisition of optical imagery and the resolution of those images has historically been limited by the ability to produce small, optically sensitive silver grains that were emulsified and coated on transparent film to form camera film. This process required chemical reactions to produce an image and was, for more than a century, the "gold standard" in optical imaging [16].

With the advent of large format charge coupled device (CCD) imaging techniques, the use of conventional photographic film has diminished and been replaced by solid-state semiconducting devices that are now ubiquitous in cameras, phones, computers, and other myriad electronic devices of the modern world. As devices have become smaller, the resolutions of these CCD cameras has become higher but remain significantly lower than the resolution of the human eye. It has been estimated that the effective static resolution of the human eye is on the order of 120M pixel, which is equivalent to a 11000 pixel by 11000 pixel array. However, the eye is in constant motion at a frequency from 75Hz to 110Hz, producing a series of images of each scene that the brain, rather miraculously, reassembles into an image that is estimated to be on the order of 500M pixels—equivalent to a 22000 x 22000 pixel array. Thus, humans constantly employ a form of super resolution imaging (SRI) to achieve our visual acuity [17, 18]. By comparison, the effective resolution of photo-emulsion film, dependent on the speed of the film, is on the order of 90000 pixels/mm^2. A direct comparison of a 35mm frame to its equivalent sized CCD array would require a pixel count on the order of 156M pixels [19]. Thus, the human eye has a significantly higher resolving capacity than photographic film and, to date, commercially available CCD cameras which can be up to 100 M pixels. This advantage is now mainly due to its SRI capability.

Since electronic imaging systems are semiconductor-based, the standard material issues associated with semiconductors have not been eliminated [20, 21]. Thus, modern CCD cameras are highly susceptible to noise from radiation sources (X-ray, γ-ray, and neutron) limiting their application in SNF storage inspection applications. Methods of producing radiation hardened microelectronics tend to drive toward larger pixel sizes in the devices while the market is driving toward smaller, higher-resolution, devices that are not intended for application in environments where the radiation is above background. In addition, the geometry of the storage casks precludes the addition of radiation shielding such as Pb to reduce γ-radiation and X-radiation. In addition, shielding of neutrons requires large quantities of hydrogenous materials such as polyethylene or water which is impractical in this application. As a result of this, the application of super resolution imaging (SRI) to this and other materials inspection problems was applied to electronic images as an analog to the process found in the human eye. A simplified description of SRI is a process where multiple lower-resolution images of a single object are acquired and then using *a priori* knowledge of the position of the camera for each image, the image is reassembled to contain the additional information combined in all of the image set to

form a higher resolution image [4]. However, there are currently a number of SRI techniques that have been discussed in the literature [6-10, 22]. Several of these algorithms increase the size of the digital storage array and fill in the added pixels using mathematical fitting, although this is not a requirement for increasing resolution, especially when other factors besides the pixel count limit the resolution of the system, such as in the fiber-optic coherent bundle.

There is ambiguity in the literature concerning the definition of resolution and the limitations on resolution that must be clarified to understand our discussion and our results. Resolution, as it is commonly defined in the classical optical literature, is limited by the spacing between the center lobe of an Airy function and its first minimum; this is called the Rayleigh criteria for resolution. The Rayleigh criteria has its origin in the mathematics that describe the convolution of a transverse electromagnetic wave (TEM), which is also known as a plane wave, with a circular aperture. Circular apertures arise from the geometry of pin-holes and lenses in optical systems and the details of the calculation are given in the literature [23, p. 352]. The resulting solution of the irradiance at a point on the image capture plane (film, CCD, etc.) is as follows for a general cylindrial optical system.

$$I(\theta) = I(0)\left[\frac{2J_1(ka\sin\theta)}{ka\sin\theta}\right] \qquad \text{* MERGEFORMAT (1)}$$

Where $I(\theta)$ is the irradiance (power/area) at an angle θ defined between the axis of the optical system at the aperture and any point off the axis, $I(0)$ is the irradiance at the center of the aperture, a is the radius of the aperture, k is the wavenumber of the light, and J_1 is an ordinary Bessel function of the first kind. The ratio:

$$\left[\frac{J_1(ka\sin\theta)}{ka\sin\theta}\right] \qquad \text{* MERGEFORMAT (2)}$$

is the function form of an Airy disk at the image capture plane of the optical system. Thus, a point source such as a star or an element of an object, when imaged on the image capture plane will have a center lobe and radiating rings due to diffraction around the edge of the limiting aperture of the optical system. The radiating rings are "noise" in the image produced by the optical system and will limit the resolution independently of the number of pixels of the image capture system (Figure 5) [24]. Thus, if an optical system has the highest number of pixels available, but the optics cannot resolve the image, the resolution is limited by the optics of the system, not the image capture component even if the system is oversampled.

If oversampling is the case in the system employed, then SRI algorithms that "fuse" the information in several images of the same pixel count can improve the resolution of the final image without increasing the pixel count in the final image. This is the case for our three image capture devices.

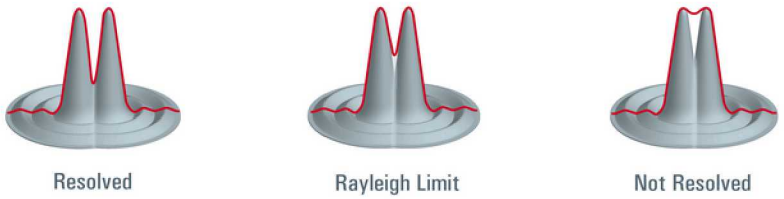

Figure 5. Example of two overlapping Airy disks and their spacing showing the resolved case; the Rayleigh limit of resolution, and the not resolved case.

SRI techniques are used to improve image quality when the captured image is "under-sampled"; that is, it not sufficiently high resolution to capture details in the true image. An example is shown in Figure 6 [24]. Each square of the images in Figure 6 represents a single pixel with a numerical value which represents the color and intensity of the pixel. This is a simplification of the actual method of data storage of the image but is illustrative of the process. In the low-resolution or "under-sampled" example (Figure 6, top), the spatial information in the object (the red checkerboard pattern) is lost in the acquired image due to the lack of pixels to differentiate between the red squares and the white squares; each pixel is pink, the average of the checkerboard colors.

If we oversample (Figure 6, bottom), there are enough pixels to save the image in a form that is recognizable as a checker board. The assumption made in Figure 6 is that all of the sampling is done simultaneously over all the pixels of the CCD analogous to the actuation of a shutter in a film emulsion camera. If we consider oversampling in space rather than in time, we can draw the illustration of Figure 7 where a one-bit low-resolution camera (black square) is used to acquire 4 images of different parts of a checkerboard and then the four images are used to produce a super resolution image with four times the resolution of the camera. Note that each square in the composite image represents one pixel which contains the color information and intensity but whose spatial extent is determined by the size of the lithographic process used in its manufacture. Thus, we get a precise checkerboard with the elements of the mathematical array assigned to the color and intensity information. Note that distortion in the color of the image of the white squares is due to the sampled area of the image containing small amounts of the red squares of the checkerboard. If exact alignment of the camera and the pixels was sampled, then the color "distortion" would not be observed. In addition, if smaller motions were sampled and many more intermediate images were acquired, then the composite image would approach the original image in resolution in the limit as the number of images goes to infinity, limited only by the Rayleigh criteria of the system.

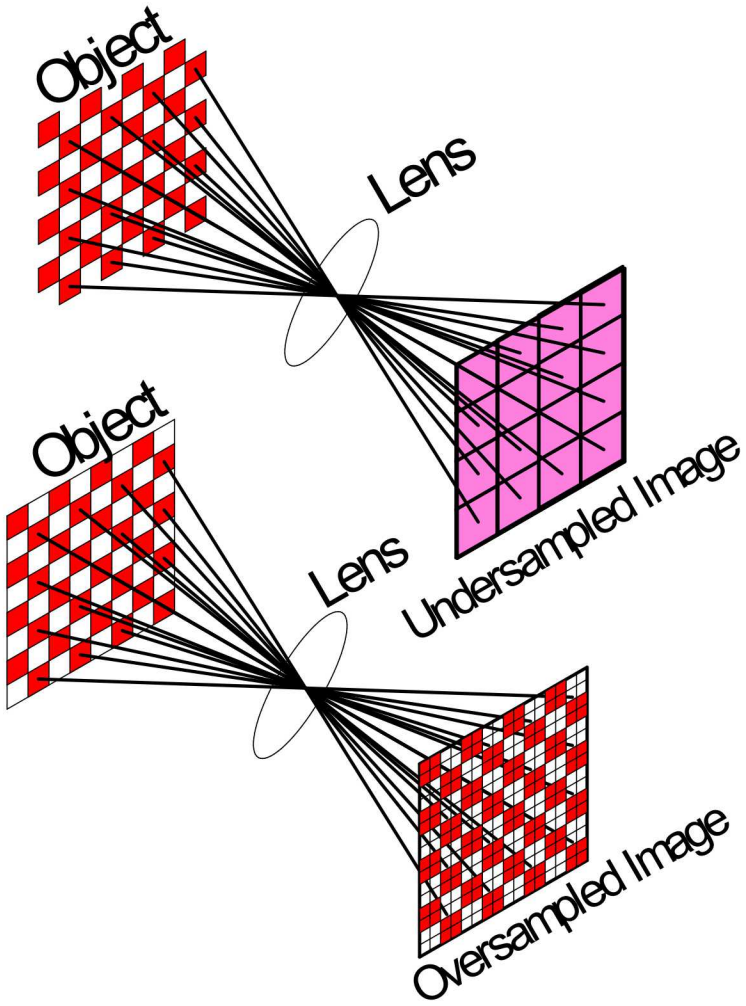

Figure 6. Illustration showing an under-sampled and an over-sampled image of the red checkerboard, where each square in the captured image represents a pixel element. The figure demonstrates that under-sampling results in loss of information, while over-sampling does not.

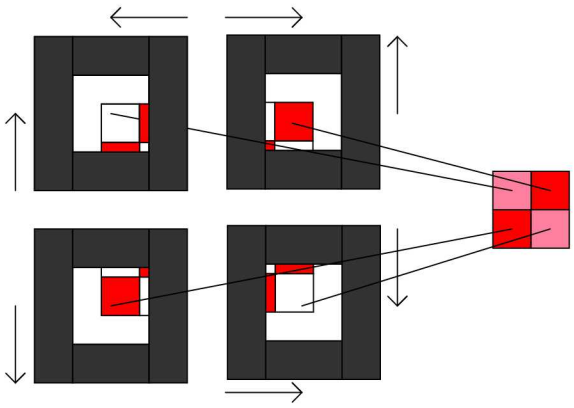

Figure 7. Illustration of a one pixel camera (black square) sampling a 2 by 2 checkerboard pattern. Although each of the four images under-samples the pattern, knowledge of the relative image locations allows combination to produce a final image that captures the spatial features of the checkerboard. The color is distorted due to the overlap of the camera and the object.

The under sampled case requires the use of SRI algorithms that do curve fitting and smoothing of the pixels and fill in the pixels in between. Thus, the final image has many more pixels than the initial raw images. The consequence of the Rayleigh criteria and result of Eq. * MERGEFORMAT (1) leads to the following relationship that is used to estimate the minimum resolvable angular separation of two objects in a system.

$$\Delta\varphi \approx 1.22\frac{\lambda}{D} \qquad \text{* MERGEFORMAT (3)}$$

In Eq. * MERGEFORMAT (3), D is the diameter of the limiting aperture of the optical system, λ is the wavelength that is being sampled (for white light, we will always use 550 nm which is the center of the visible range and effective peak of the spectrum of the sun) and *1.22* is a constant that is derived from the angular spacing of the center lobe and the first minimum of the Airy function (Eq.* MERGEFORMAT (1)). The three cameras of Table 1 were analyzed and the minimum angular separation was calculated in Table 1 for a nominal separation of 1 cm from the surface. Each of the cameras is at the limit of the Nyquist criteria for spatial sampling at a 1 cm spacing since Nyquist requires a minimum of two samples for the highest frequency in the sample. The width of the SCC cracks is 30 µm which requires a ~15 µm sampling interval. Thus, SCC algorithms that maintain the same number of pixels as the raw data should be oversampled enough to have improvement by these less complex algorithms if the spacing between the entrance optic and the surface is kept at a distance less than the 1 cm criteria. Consideration of the geometry for the SNF casks demands this due to the tight spacing available.

Table 1: Comparison of the minimum angular separation and minimum feature size that can be resolved for the three instruments tested.

Camera Model	Lens Diameter (mm)	Δφ (μ radians)	Min. Feature at 1cm (μm)
Hawkeye Pro	4	170	17
Dino-Lite Primer II	3	230	23
GE - Everest XLG3	5	130	13

Thus, by combining multiple images taken at different locations or angles, it is possible to build a composite image that has higher resolution than any of the individual images used to construct it. Three steps are involved in the process. First, each individual image is preprocessed to remove imaging artifacts. Then the images are registered and other individual features of interest are aligned with each other. Finally, the images are combined and normalized together to make the higher resolution composite image. Each of these steps is described below, as it was implemented in this project.

3.2. Preprocessing

One of the issues that arises in any optical inspection system is the distortion of the image from the optical system itself. Even with the application of very-high quality optical systems, distortion due to spherical aberration, chromatic aberration, and other limitations of the optical system result in reduction of the resolution of the image. Very high-quality optical systems generally require the combination of several lenses in series to compensate for aberration and thus, require a large volume. The physical limitations in the SNF container preclude the addition of complex lens systems. For the simpler lens systems, additional distortions related to lens quality are important. For the systems we tested, lens distortion, in particular barrel distortion and chromatic aberration, were especially significant.

An example of these effects is provided in Figure 8. The image is of a black grid on a white background, and while the center of the grid is sharp and the lines are straight, the lines become concave, bowing outwards as the edges and corners of the image are approached (Figure 8a); this is illustrated in an exaggerated fashion in the inset. At the corners of the image, a blurring also occurs, illustrated with close-ups in Figure 8b. This is due to both spherical aberration and chromatic aberration. Spherical aberration is a loss of definition at the edges of an image, caused by differences in where light focuses when it passes through the edge of the lens rather than the center. Chromatic aberration is due to differences in the refractive index of light as a function of the wavelength, or color, of the light; for light passing through the edges of the lens, the colors become increasingly separated. In Figure 8b, this shows up as yellow and blue fringes on the white squares that are separated from each other in the direction away

from the center of the image. The fringes overlap the black lines, making them less sharp.

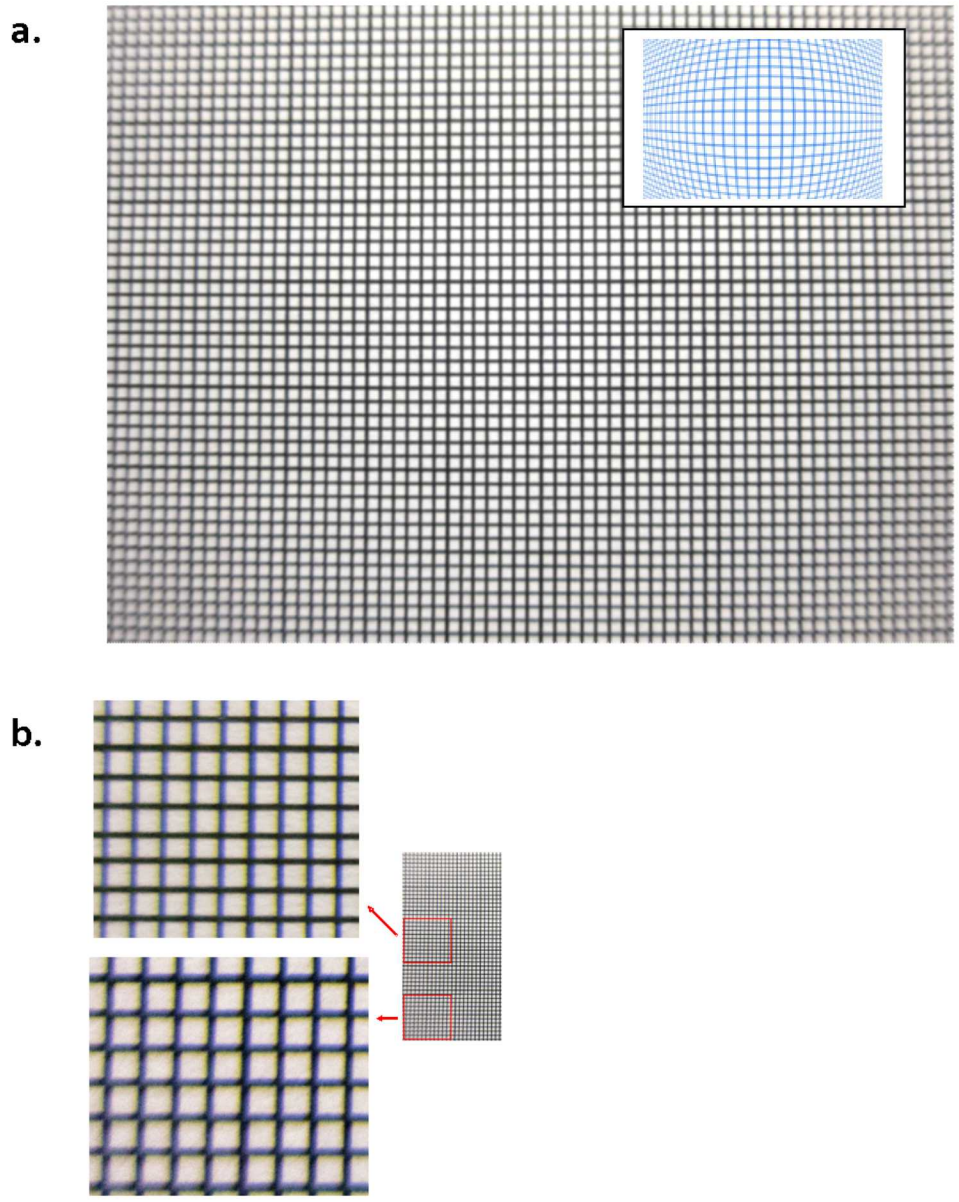

Figure 8. Color image of Black and White Grid, Showing Barrel Distortion (a) and Chromatic Aberration (b).

Barrel distortion is a common problem exhibited by microscope lenses such as those used here, as they are wide-angle to capture the close-up image at a short working distance. An example of this was images captured with the Hawkeye fiber optic borescope, for which the end of the fiber bundle was captured via a lens with a CCD camera. A borescope image is shown in Figure 9 on the left side; for scale, the vertical line extending from the vee at the top of the image to the tip of the "L" is a

one mil (25um) diameter Au bond wire. The top of the lettering should be a straight line, but as evidenced by the red line, there is significant curvature to the tops of the letters. This can be compensated for by using a MatLab script to measure lens correction parameters, and to apply them to the image. This is outlined in the article on camera calibration found on the MathWorks web site [25]. The process produces an array of values called "cameraParms" and then each image from the particular camera is corrected by adding the following line of code in the Matlab script.

$$IM\_Corrected = undistortImage(IM\_Initial, cameraParams);$$ * MERGEFORMAT (4

In the above Matlab line, the original image (*IM_Initial*) is corrected for barrel distortion using the Matlab function "undistortImage" and the derived "cameraParams" to produce the corrected image (*IM_Corrected*).

The result of using this algorithm is seen in the right-hand image of Figure 9; the text is no longer distorted, and aligns with the red line. The same routine was used with all the image capturing devices that were tested.

Figure 9. Photograph of lettering using the Hawkeye borescope. Left: barrel distortion is visible as curvature of the lettering. Right: following correction using the MatLab script (right image), the distortion is gone.

Chromatic aberration occurs because spherical aberration differs with the wavelength of light, resulting in color fringes at the edges of the images. It cannot be corrected for entirely. Converting the image to gray scale, or even capturing it as gray scale, does not remedy the effects of chromatic aberration, as it occurs when the image passes through the lens prior to capture by the CCD. Algorithms exist for correcting chromatic aberration, but they cannot restore information lost due to overlapping color fringes. One potentially useful approach is to use a monochromatic light source. We attempted this with a ring of narrow wavelength diodes as a light source around the camera. Although a promising approach, initial attempts did not yield uniform lighting (the diodes produced light rings), and there was insufficient time to solve this problem.

In the case of the coherent fiber optic cable, an additional Fourier spatial filter preprocessing step was carried out, to reduce the pattern caused by the individual fibers. This is discussed in Section 4.3.2.

It is important to correct for lens aberrations to the greatest degree possible prior to combining images in SRI processing. First, if image registration is being done automatically, then distortion of features in the image could result in poor registration. Second, even if registration is as good as possible, distortion of features will negatively affect the quality of the final combined image.

3.3. Registration

The ability of any algorithm to reassemble an image is inherently tied to the knowledge of the location of the object and the orientation/location of the camera. Consider the SRI algorithm applied by the human brain. The brain must have the additional information about the direction that the eye is pointed along with the ability to store the image from previous frames acquired in order to produce the final image which we interpret as one image of the scene. SRI algorithms include a first step in which the images are compared and aligned with each other, via translations such as shifting, rotation, stretching, or distortion (e.g., correction for perspective) in order to align features in the suite of images. The images are then combined, as described in the following section.

It is the thesis of this project is that by controlling camera movement and using exact knowledge of camera translations to shift and register the images will result in the optimal SRI combined image. We tested this using automated image registration tools, and found that the final image quality was indeed better when we used *a priori* knowledge of camera translations to register the images. Comparison of the raw data acquired from the borescope on a resolution target to a cubic spline SRI algorithm and our translation SRI algorithm is given in Figure 10 which shows a marked improvement in the image quality in the translation SRI image (c) compared to the raw data (a) and a cubic spline interpolation SRI algorithm (b).

a.

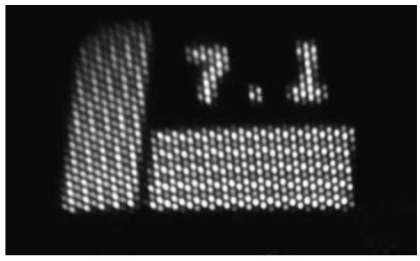

b.

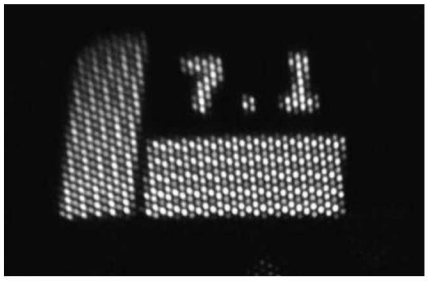

c.

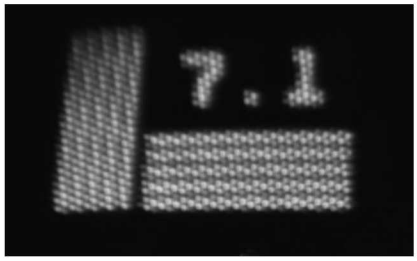

Figure 10. Comparison of a resolution target acquired using the Hawkeye borescope fiber optic camera with two different SR algorithms. (a) raw image showing the individual pixels; (b) result of a cubic spline interpolation algorithm that automatically registers the images; (c) result of our SRI algorithm, which exploits prior knowledge of the camera.

3.4. Image Combination

Mathematically, the two-dimensional acquisition of an image on a CCD camera can be written as follows:

$$g(x,y) = f(x,y)\sum_{n=1}^{N_x}\sum_{m=1}^{N_y}\delta\left(x-nX_o\right)\delta\left(x-mY_o\right) \text{ \\* MERGEFORMAT (5)}$$

In the above, the projected image of the object scene is $f(x,y)$ and the Dirac delta sampling function in either dimension is $\delta(x-nX_0)$ for the horizontal dimension and $\delta(x-mY_0)$ for the vertical dimension where X_0 and Y_0 are the center to center spacing of the pixels in the x and y dimensions respectively. In addition, N_x and N_y are the number of columns and rows of the CCD array respectively. If we Fourier transform Eq. * MERGEFORMAT (5) in two dimensions the result is as follows:

$$G(u,v)=\int_{-\infty}^{\infty}\int_{-\infty}^{\infty} f(x,y)\sum_{n=1}^{N_x}\sum_{m=1}^{N_y}\delta(x-nX_o)\,\delta(x-mY_o)\,e^{-2\pi j(ux+vy)}dx\,dy \quad \text{* MERGEFORMAT (6)}$$

Which we recognize as the convolution of the two functions in the spatial frequency domain:

$$G(u,v)=F(u,v)\otimes\sum_{i=-\infty}^{-\infty}\sum_{k=-\infty}^{\infty}\delta(u-iU_0)\,\delta(v-kV_0) \quad \text{* MERGEFORMAT (7)}$$

Where U_0 and V_0 are the sampling frequency in the horizontal and vertical directions and correspond to the spacing of the CCD pixels in the two directions. Examination of the right-hand function in Eq. * MERGEFORMAT (7) implies that the sampling function will replicate itself in the frequency domain with a replication frequency of U_0 and V_0 for the horizontal and vertical directions respectively. If we then consider the highest spatial frequency contained in the sampled image as U_H and V_H, then U_0 and V_0 must be a minimum of $2U_H$ and $2V_H$ in order to keep the convolution ($G(u,v)$) from overlapping in the frequency domain. This is the origin of the Nyquist sampling criteria that requires sampling of a minimum factor of two higher than the highest frequency in the sample. If the convolution overlaps, then the spatial information is lost as illustrated in the upper part of Figure 6 [26].

Figure 11 is an illustration showing this point where a single vertical frequency is sampled across the horizontal axis. In Figure 11, the highest horizontal frequency (U_H) of our notional function $G(u,v)$ is less than ½ U_0, as such, no distortion between the replicates of the convolution occurs. However, if $U_H \geq 1/2U_0$, then the replicates overlap due the sampling function and we lose spatial information in our image.

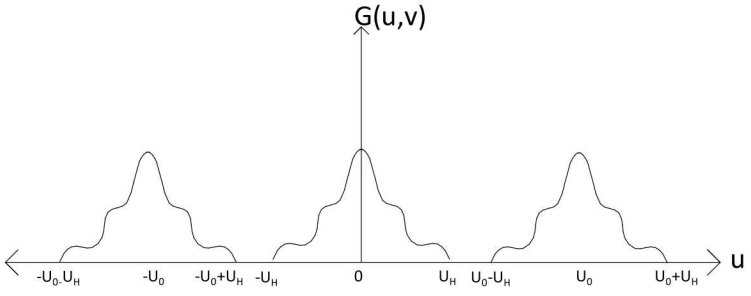

Figure 11. Illustration of the sampling of the image in spatial frequency space showing that if the highest frequency of the image is less than ½ of the sampling frequency U_0, then the replicates will overlap and the signal will be distorted.

4. BENCHTOP TESTS

The initial step in the project was to build benchtop systems for testing different imaging systems and camera motions, and for SRI processing algorithm testing and development. This first step was necessary in order to determine the most effective camera motions, and the required specifications for the prototype imaging stage. The benchtop tests required building stages with adequate controls on camera or sample motion (in many tests, the camera was fixed, and the sample was moved); developing or acquiring SCC samples for testing purposes; and acquiring imaging systems for testing.

The benchtop system was used for testing of different types of camera motion, for developing algorithms to best process data for each camera motion, and to evaluate the relative benefits of each on the quality of the SRI images produced. Given the limited duration of the proposed program, camera translations were limited to one degree of freedom. Translations that were evaluated included camera rotation and lateral translation while viewing from above. The high resolution of the stage also allowed use of sub-pixel lateral translations, to evaluate the benefits of small camera steps. Camera/pixel orientation relative to the feature of interest was also explored. Stress corrosion cracks are linear, branching features, and it is likely that feature orientation relative to translation direction will significantly affect the level of improvement afforded by SRI processing. The benchtop system was also used to test the benefits of different lighting angles. For a camera, variations in lighting angle are readily achieved by use of a ring of controllable light-emitting diodes around the camera lens. A ring of diodes could also be used to illuminate the area of interest for a fiber-optic bundle system, but an alternative is to send the light directly down the bundle, masking off different parts of the bundle to get different lighting angles. Lighting conditions turned out to be strongly dictated by the high specularity of the metal surface, which inhibited imaging, and enforced some lighting choices.

4.1. Testing Stages

The benchtop systems were based on two repurposed stages, one a high accuracy X-Y stage with sub-micron X-Y resolution, and the second, a ThorLabs model CR1-Z7 rotation stage which is rated for precision of 5 arcmin. The stages could readily be reconfigured and electronically controlled for arbitrary step sizes. One of the stages is shown in Figure 12. For *in situ* inspections, the camera would be moved over a stationary metal surface; however, for testing purposes, it was frequently better to fix the camera in position, and to use the stage to move the sample in front of it.

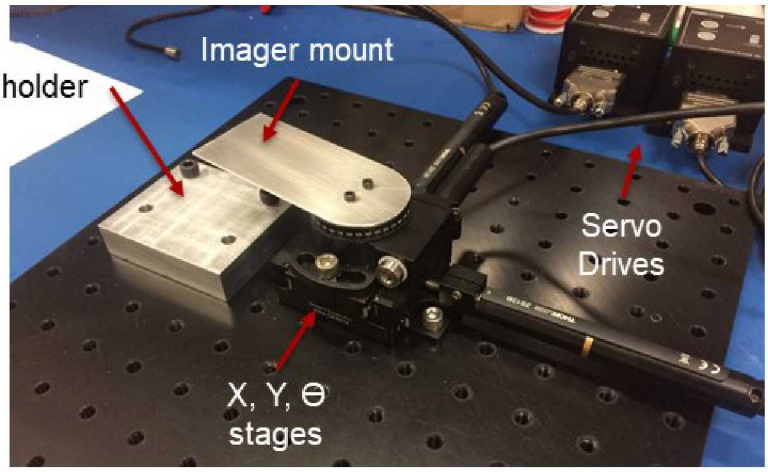

Figure 12. Stage for benchtop imaging system

4.2. SCC crack test samples.

In order to perform relevant benchtop tests, representative SCC cracks had to be obtained. Three different types of specimens were used.

- An archived SCC crack specimen from the Yucca Mountain Project (Figure 13a). This specimen consisted of a circular plate 10" in diameter and ¾" thick, with two braces welded to the bottom, and then a full-thickness axial weld bisecting the plate. After manufacture, the sample was exposed to boiling saturated magnesium chloride (~155ºC) to induce SCC cracks. This produced large cracks, and suite of smaller cracks, near the weld. The smaller cracks were extremely narrow, and good analogs for SCC cracks formed by atmospheric corrosion in the field. The boiling magnesium chloride method, however, produces rust staining that marks the cracks in a manner that may not occur under field conditions.

- Standard SCC U-bend samples (Figure 13b). The U-bend samples were made of 304L stainless steel acquired from Metal Samples Company (USA). The U-bend coupons had a 120 grit finish and measured 5" long, ¾" wide, and 1/16" thick; the specimens were bent with a ½" radius. $MgCl_2$ droplets were deposited on the specimens prior to exposure at salt loading levels exceeding 500 µg/cm^2. The salt-loaded specimens were exposed to 35% relative humidity (RH) and 65ºC for 1 month. After exposure and prior to inspection imaging, the rust on the samples was removed by gently brushing with an aqueous diammonium citrate solution (150 g/L) followed by a water rinse and air dry. For use in the tests, the samples were wrapped around a ½" mandrel, and the mandrel was rotated in discrete steps, while the camera was held fixed.

- A 4-point bend specimen (Figure 14). SCC crack widths are controlled by plastic and elastic strain rather than removal of material via corrosion, and are determined by the level of stress in the sample and by the thickness of the sample. To duplicate what is expected to occur in SNF interim storage

canisters, we constructed a 4-point bend apparatus, based on a design developed by the Colorado School of Mines. The specimen plate used in the apparatus, is 12.6" long, 4" wide, and 5/8" thick (SNF dry storage canisters are mostly either ½" or 5/8" thick). The specimen was loaded to produce ~ 200 MPa tensile stress on the exposed surface, similar to what is expected for weld residual stresses in SNF storage canisters [27]. The stressed region of the specimen was coated with magnesium chloride brine, seawater, and NaCl at four different salt loads. After 2 months in an RH chamber at 80ºC and 40% RH, heavy corrosion was observed, especially in the quadrant where magnesium chloride brine was deposited (Figure 14). However, once cleaned to remove the rust, no SCC cracks were visible. There was insufficient time to make a second attempt.

a.

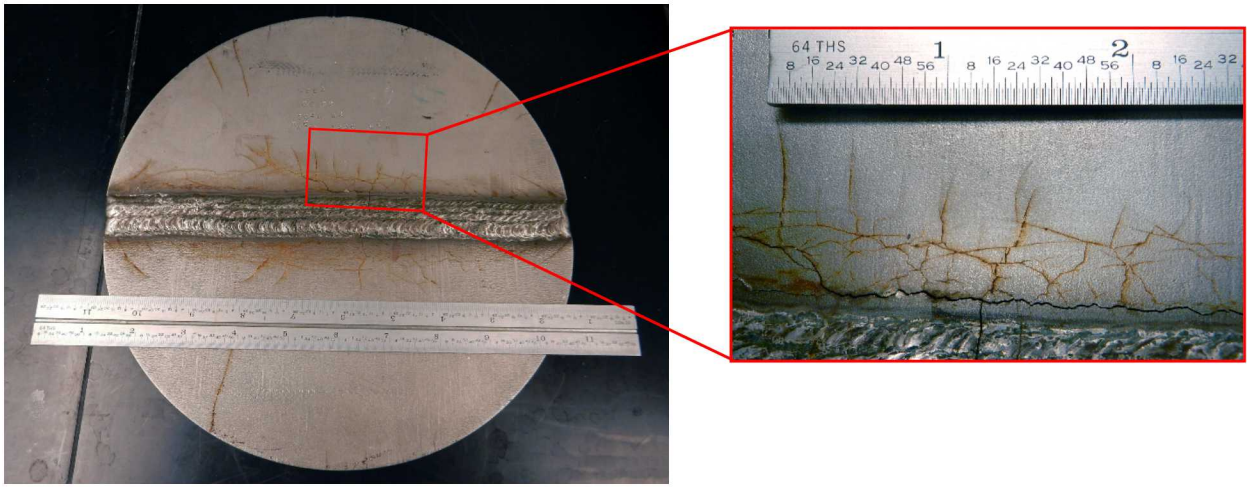

b.

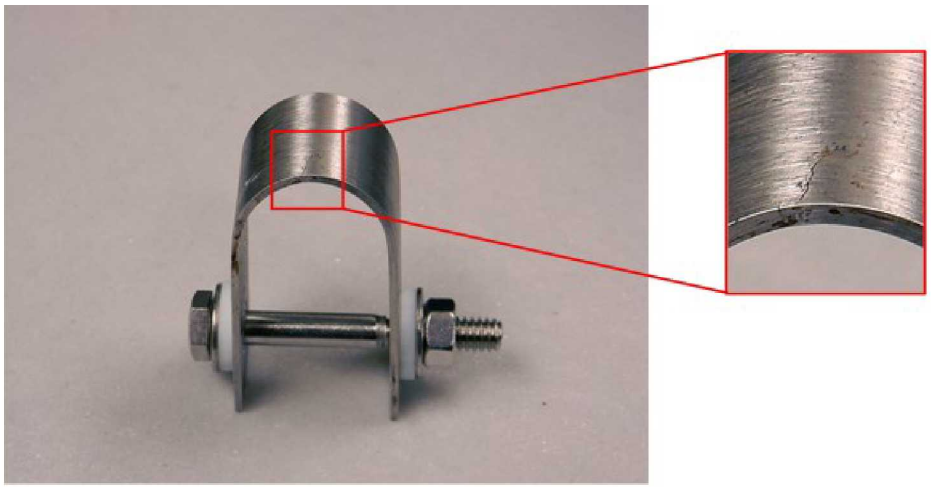

Figure 13. Large plate (a) and U-bend (b) SCC test samples.

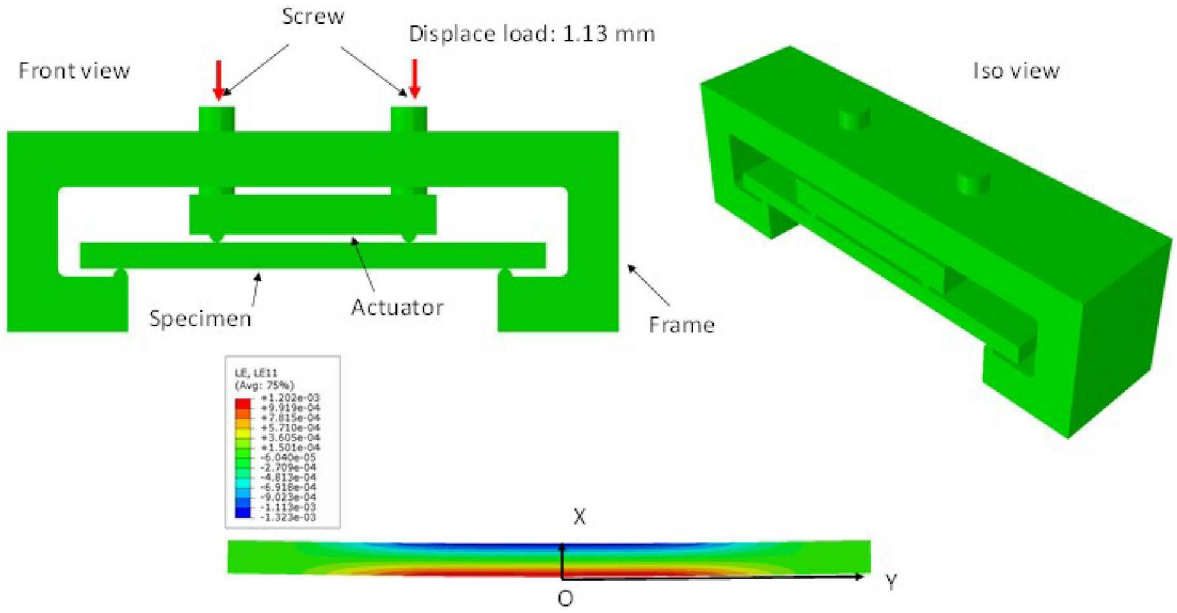

a.

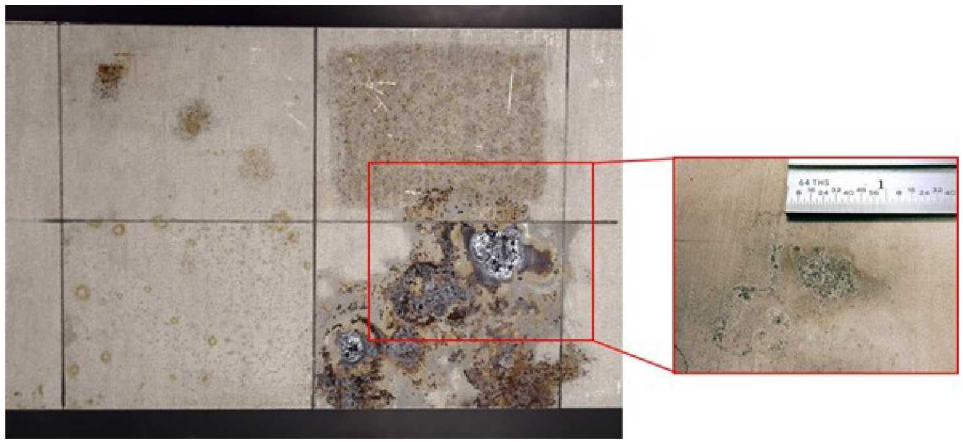

b.

Figure 14. Four-point bend specimen. Apparatus design (a) and uncleaned and cleaned sample (b).

4.3. Imaging units tested

As described below, three different imaging systems were used. Initial experiments were done with a Dino-Lite Digital Microscope, and with a Hawkeye coherent fiber optic borescope, that combines a coherent fiber optic cable with a small digital CCD camera to capture the transmitted image. The digital microscope camera had a significantly higher resolution, and was used as an analog for a CCD-based camera that might be used in field applications. Coherent fiber optic-based imaging systems are frequently used in high radiation environments that would damage a CCD-based camera. However, their weakness is that limits in the diameter of the individual clad optical fibers greatly limit the resolution of the devices. The coherent optic fiber used here had approximately 18,000 separate fibers, and was one of the highest resolution coherent fiber optic imaging systems available—considerably higher resolution coherent fiber optic borescopes are made, but have short, rigid sheathed cables, unacceptable for this application.

After several months of testing, we obtained, on loan, a GE Inspection Technologies XLG3 Videoprobe, with a GE XLG3T84120SN imaging tip. This probe has been used in many canister inspections to date, and we designed the eventual imaging module that we constructed to utilize this instrument. The final benchtop tests were used to familiarize ourselves with this instrument, and to test the effectiveness of the SRI processing algorithms we had chosen based on the initial experiments. GE loaned us the instrument free of charge; however, as discussed in Section 7, difficulties in settling on the wording of the loan agreement delayed the delivery of the instrument for 3 months, significantly impacting our schedule.

4.3.1. Dino-Lite Digital Microscope

Testing with the Dino-Lite Primer II digital microscope involved acquiring images while translating the sample material with a precision rotation stage. The U-bend samples described in Section 4.2 were used as test samples. Because they maintain their shape and cannot be placed on a horizontal surface to be imaged, a 3-D printed mandrel was constructed and placed on the ThorLabs model CR1-Z7 rotation stage (Section 4.1) and rotated to acquire the data set. Images were collected in groups of 10; since the radius of the mandrel is about 5 cm, 10 images cover about 0.5 mm. The results illustrate that the microcracks are of sizes less than 30 μm.

A fundamental element of the inspection system we propose for SNF inspection is a robot to transport our optical system to a known position in the volume of interest and then acquire optical information at known positions for re-assembly into SRI images. An example is given below for a single frame (Figure 15) taken from a Dino-Lite Primer II digital microscope and a corresponding SRI image of the same scene, made by combining 10 frames, each shifted by 50 μm. The image in these figures is of a U-bend corrosion test sample. Close examination of Figure 15 shows cracking but only the largest of the features are visible in the image. However, by combining 10 separate images that are spaced a known amount apart (~50 μm), we can produce the image of Figure 16 which shows a number of "hairline" cracks that are invisible in the single image. Thus, a system with a precision translation mechanism (robot, etc.) can

be used to place the camera in multiple locations for collection of images which are then combined using a computer and software to produce an image with much higher resolution. The requirement of a precision translation is implied in the performance of this approach.

All of the algorithms that will be discussed are based on MatLab [28] and employ the functions *imfuse(A,B)* which creates a composite image from two images, A and B and *imtranslate(A,translation)* translates image A by the translation vector specified. The translation vector is a two-element array in Matlab whose first element is the value of translation in the horizontal and the second element is translation in the vertical direction.

Each image is read into the program and then translated by the translation vector as determined from *a priori* knowledge of the translation of the camera between images. Each new image is added via the function *imfuse* to produce a composite image of the two previous images. The images of Figure 15 and Figure 16 are processed after previously being converted from red green blue (RGB) formats to black and white (BW) via the Matlab function *rgb2gray(A)* which produces a 256-bit gray scale image from a colormap of the image.

The above discussion relies on a qualitative observation of the improvement in the visiblity of the cracks due to the processing algorithms. However, it is useful to attempt to quantify the improvement in the image. To do this, we evaluate the change in resolution (signal-to-noise ratio, or SNR) that results due to processing. Consider Figure 17, which shows an image of two cracks. If we draw a horizonal line across the image, we can plot the magnitude of the grey scale as a function of pixel position. This is shown in Figure 18. For the original single image (black line), we see that the two cracks have signal-to-noise ratios of about 2 and 1.5 as we move from left to right across the picture. The red line in Figure 18 is a cross-cut of the image after 10 images were combined using SRI algorithms, and we see a substantial improvement in the SNR of 7 and 10 as we process from left to right. This implies an improvement in SNR of about 5 times as a result of SRI processing of 10 individual images.

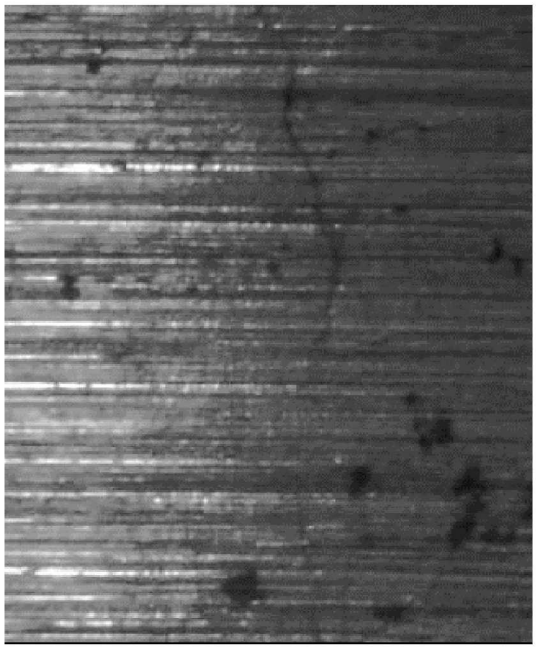

Figure 15. Single image of a SCC crack imaged by the Dino-Lite Premier II microscope.

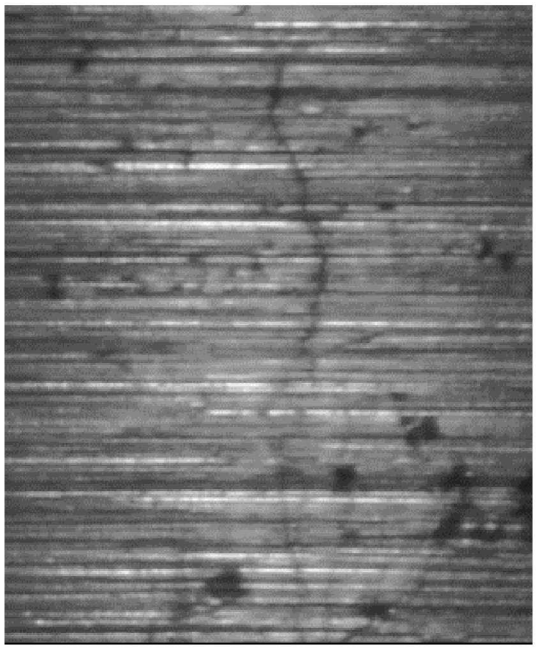

Figure 16. Composite image produced by SRI combination of 10 images, each shifted 50 µm in the horizontal direction relative to the last. Additional fine cracks are visible that were not visible in Figure 15.

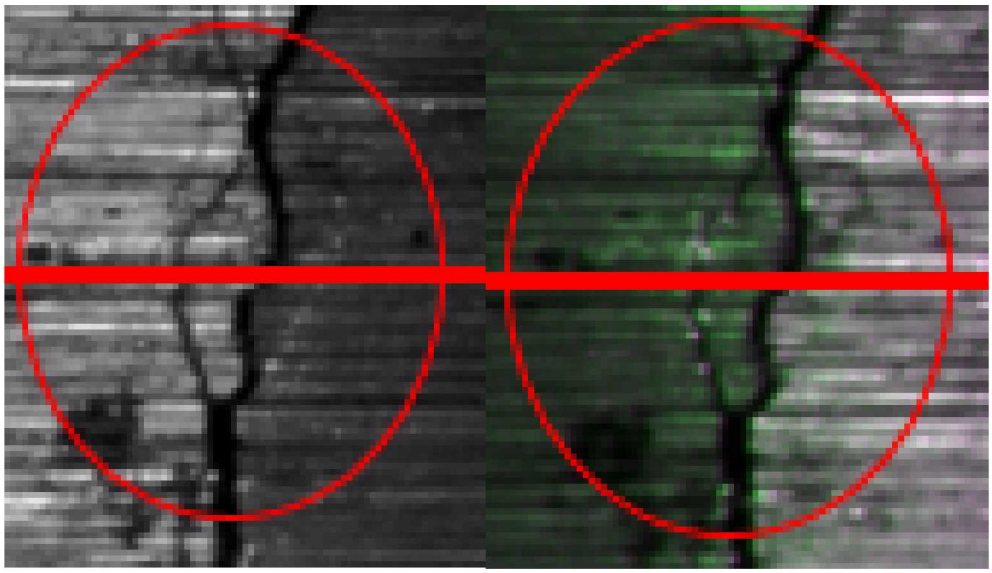

Figure 17. Cross-cut of the a crack in a raw image (left-hand) and an SRI processed image (right-hand). Red horizontal line is cross-cut of the sample. Data acquired with Dino-Lite instrument.

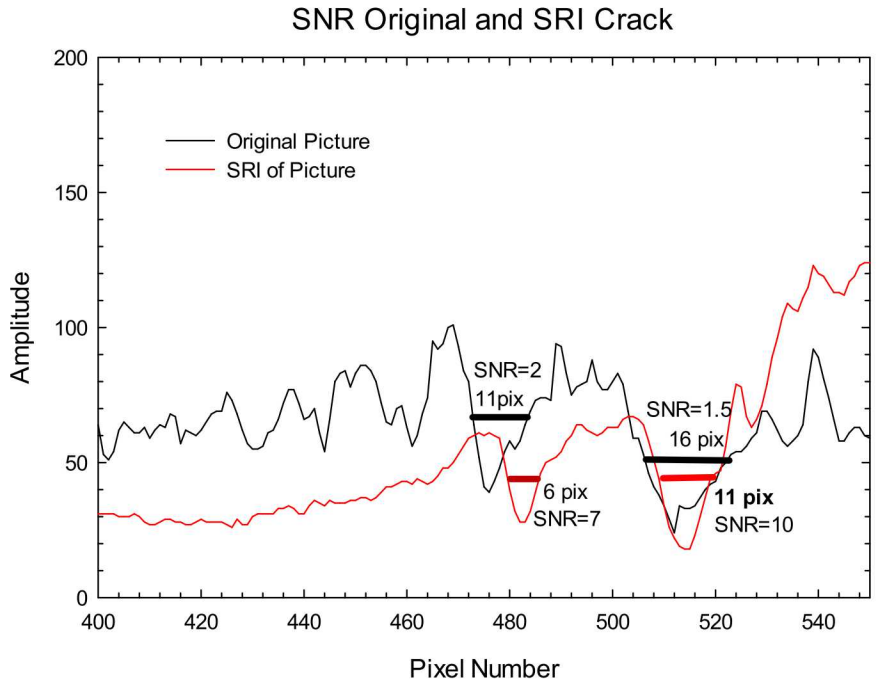

Figure 18. Plot of improvement in SNR due to the SRI processing in the Dino-Lite. Black—single image, red-SRI image using 10 samples.

4.3.2. *Coherent fiber optic cable*

As discussed previously, in settings such as the surface of a spent nuclear fuel storage canister, high radiation levels may limit the functionality of a CCD-based imaging system. Not only does radiation cause image degradation (noise) in CCD-based systems, it eventually damages the CCD camera itself. One option for allowing access to the region around the SNF cask, is the use of a coherent optical fiber bundle which transmits the image to a camera on the exterior of the cask, where the radiation is much lower and there is room for bulky, complex hardware.

A notional drawing of a coherent fiber optic bundle is shown in Figure 19 which shows a letter "H" being focused on one end of the bundle and the resultant transmitted image. The bundle consists of many individual optical fibers whose orientation is maintained with respect to each other over the length of the bundle. Thus, a small fraction of the image light that impinges on the entrance side of the bundle is transmitted to the exit side of the bundle as a single pixel of the bundle. Since the fibers are significantly larger than a pixel on a CCD array, there is loss of resolution in the system as illustrated by the transmitted "H" in Figure 19.

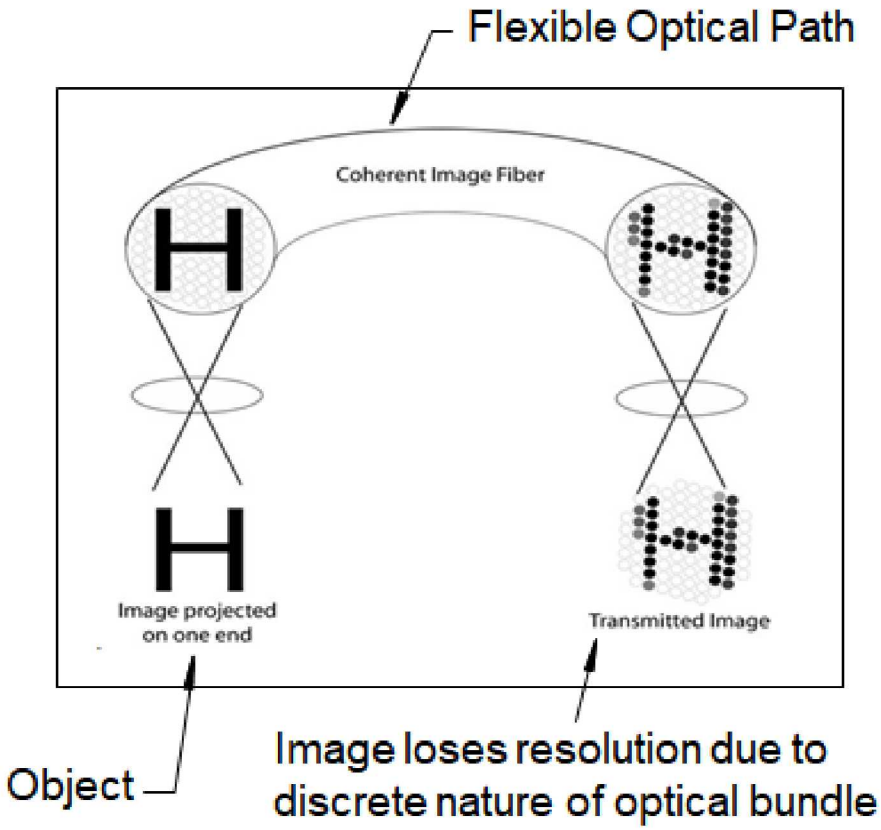

Figure 19. Coherent fiber optic bundle.

Despite the relatively low resolution of coherent fiber optic borescopes, the resistance to radiation damage makes them an attractive alternative for some applications. For this reason, the second type of camera that was tested was the previously mentioned fiber-optic borescope (Hawkeye Pro PFB4 with Color Camera Module XC-505). The fiber borescope employed in our measurements has 18000 fibers in a 4 mm diameter area for a "pixel" spacing on the order of 26 μm or a pixel density of 1400/mm^2. This is by far the lowest resolution instrument tested and would have no application to this problem were it not for the inherent radiation hardness of the system and its ability to be inserted into the volume to be inspected.

Optical fibers are made of fused silica that has a low level of dopant in the center "core" of the fiber to produce a slightly higher index of refraction in the core. Thus, for incident light angles above the "critical angle" [23], total internal reflection occurs and the light is confined to the core of the fiber. Thus, a portion of a scene that is viewed in the acceptance angle of the fiber is transported to the end of the fiber. Since the fiber is cylindrical and will not support transverse electromagnetic modes [29], the spatial information at the entrance of the fiber is "scrambled" resulting in a single color "pixel" at the exit as alluded to in Figure 19. Fused silica is substantially more radiation hard than semiconductors although it is damaged by radiation and will eventually become more lossy due to radiation exposure [30, 31].

The low-resolution of the fiber bundle is the limiting factor in the applicability of the fiber system to find SCC features. Figure 20 shows the image of the same sample imaged by the Dino-Lite Microscope in Figure 16, but the very fine cracks seen with the Dyno-Lite microscope are not visible using the optical fiber array. A SRI image of this same crack, again compared to the Dino-Lite image, is given in Figure 21 and illustrates the ability to decern the smaller cracks in the material. Figure 21 was constructed from a series of 10 images at the resolution of Figure 20, along with the correction for barrel distortion. Comparison of the two figures illustrates the improvement in the ability to image cracks when using SRI processing techniques, and demonstrates the viability of the application of SRI to the problem of canister inspection.

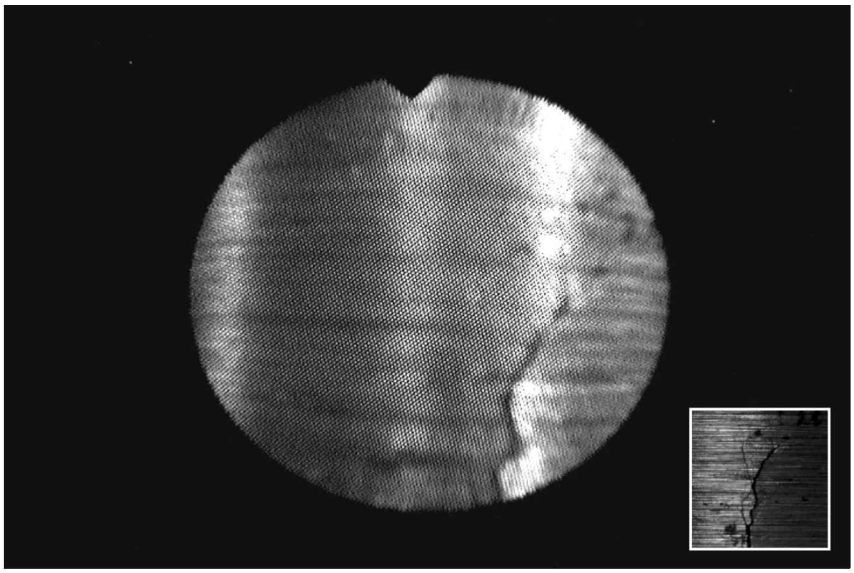

Figure 20. Image of a crack through the fiber-optic coherent bundle showing a large crack (lower left). Inset: The same crack, imaged using the Dino-Lite camera.

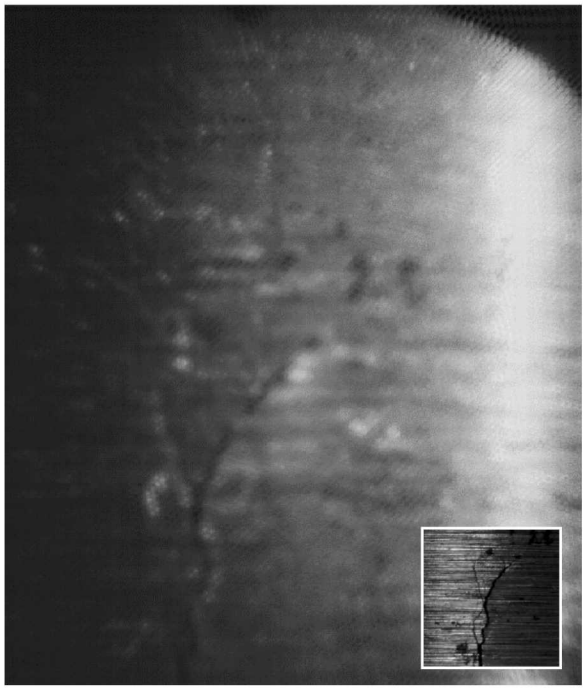

Figure 21. SR image the same crack, made by combining 10 images to improve the resolution of the photo. Note the appearance of the additional cracks that are not visible in the single image. Inset: The same crack, imaged using the Dino-Lite camera.

Although Figure 21 shows a significant improvement in the ability to resolve small SCC cracks, the quality of the image is still low; this is because of the pattern created by the individual fibers. To reduce the pattern of the individual fibers, a second digital signal processing algorithm was applied to the images from the borescope prior to combining them. The process involved first calculating the two-dimensional fast Fourier transform (FFT) of the stored image using the following code:

FImage=fft2(Image_BW); * MERGEFORMAT (8)

This Matlab script first converts the image a black and white image (*Image_BW*) and then calculates the FFT and stores it as image "*FImage*." For a typical image, the FFT looks like Figure 22. The strong hexagonal pattern results from the hexagonal closest-packed fibers with their sheaths. The next step is to calculate a binary mask by making a matrix that has values of "zero" for signals above a set threshold and "one" for values below that threshold. This was done using the following function call, where the variable "*amplitudeThreshold*" is determined heuristically.

$$F\_mask = \log(1 + abs(F\,\mathrm{Im}\,age)) < amplitudeThreshold; \quad \backslash^* \text{ MERGEFORMAT (9)}$$

The result is a binary mask such as what is shown in Figure 23,where the white pixels are binary "ones" and the black pixels are binary "zeroes." The square in the middle is the two-dimensional low-pass filter that allows all of the low frequency data to remain while selectively removing the frequencies that result from the close-packed individual fibers. The final calculation is to multiply the FFT of the image and the digital filter on an element by element basis, and then reverse FFT the result. The MatLab script for this is given below:

*Processed_Image=FImage.*F_mask;* * MERGEFORMAT (10)

It should be noted that in Matlab, the operation ".*" does an element by element multiplcation rather than a standard matrix multiplication. As an example of this process, a single raw image of a metal surface without any known crack or important features from the Hawkeye borescope is given in Figure 24, and the corresponding image, after filtering using the FFT generated digital filter is given in Figure 25. By combinging FFT filtering with SRI imaging a singificant improvement in image quality results. This is shown in Figure 26, in which a single raw image from the Hawkeye borescope is compared to a SRI image produced from a set of FFT-prefiltered images. The pre-filtered SRI image on the right shows substantial cracking that is not observed in the single image on the left.

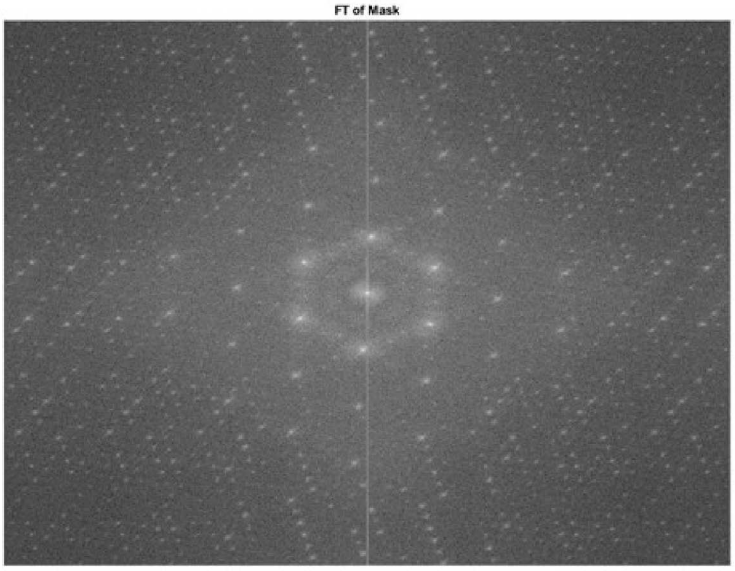

Figure 22. Two-dimensional Fourier transform of a fiber image. The period structures in the image are due to the pixelation of the image from the fiber bundle.

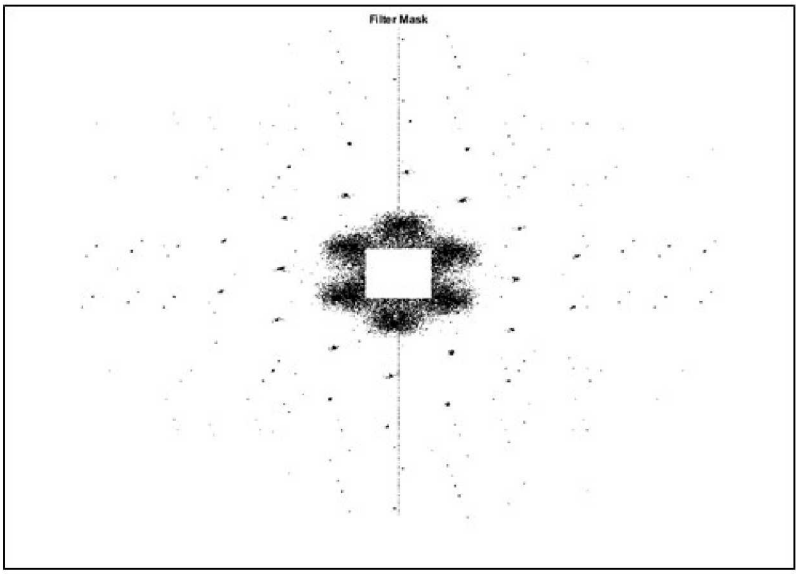

Figure 23. Digital filter used to remove the pixelation in the fiber images.

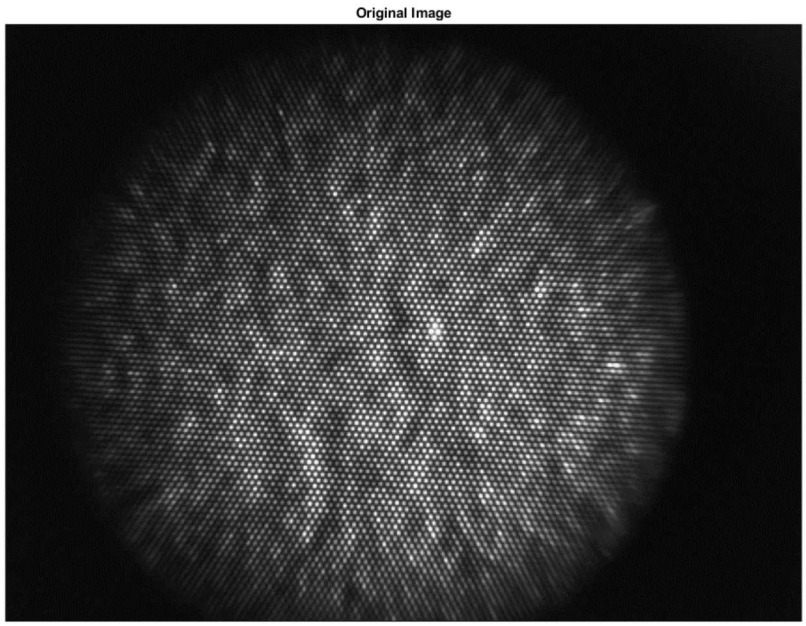

Figure 24. An image of a metal surface acquired using the borescope showing the pixelation from the borescope.

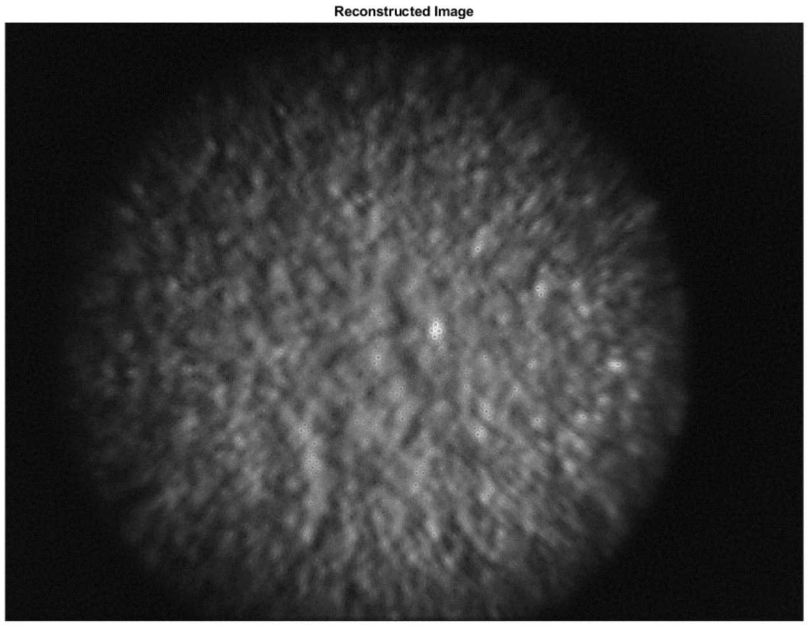

Figure 25. The same image, showing the pixelation removed using the digital filtering algorithm.

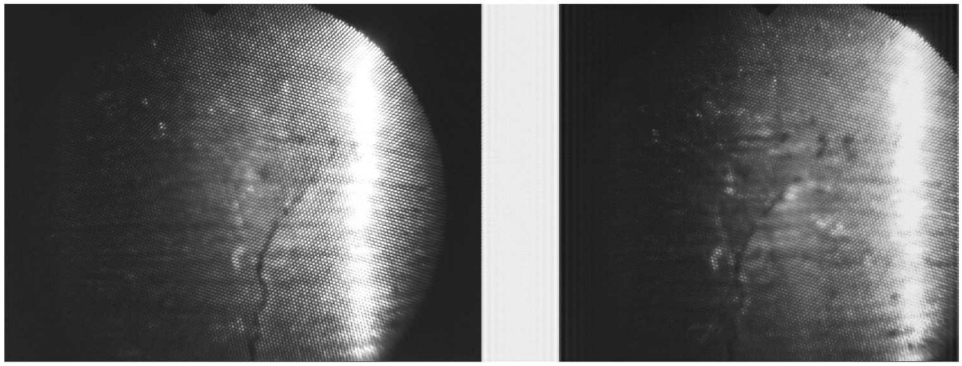

Figure 26. Combined SRI image with FFT pre-filtering of cracked metal. Illustration shows more and finer cracking on the right hand image after processing.

4.3.3. GE videoprobe

The third camera that was tested was a GE - Everest XLG3 probe with a 5 mm input aperture and 440000 pixels. Similar measurements were acquired of cracks and then processed using the above algorithms. An example of a single image and an SRI image from the GE probe is given in Figure 27. As the quality of the single image, at least as reproduced by the computer, is very good and it is difficult to see any improvement due to SRI. However, by doing a cross-cut of the same crack imaged in Figure 17 with the Dino-Lite camera, we can compare the improvements in the SNR of the image. This is done in Figure 28 and illustrates an improvement of about 30% between the processed and the unprocessed images for a 10 image SRI sample. This improvement is less than what was observed in Figure 18 for the Dino-Lite camera but still greater than for a single image.

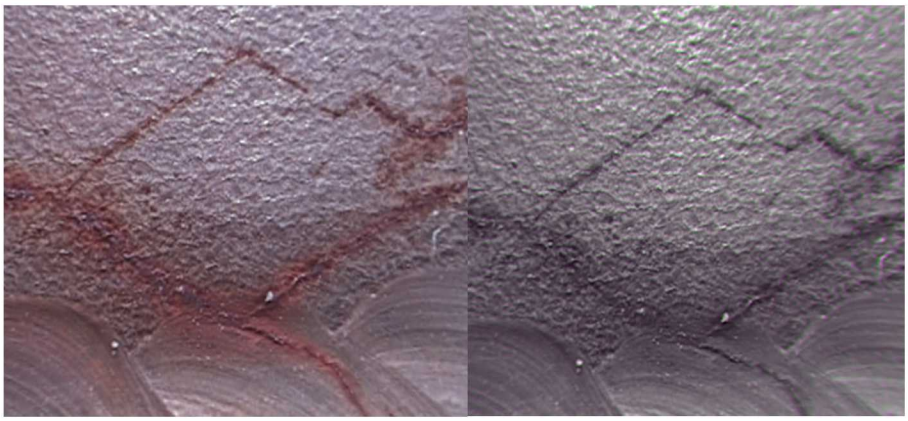

Figure 27. Example of crack images acquired using GE system. Left image is a single image and right image is a 10 image SRI composite image of the sample.

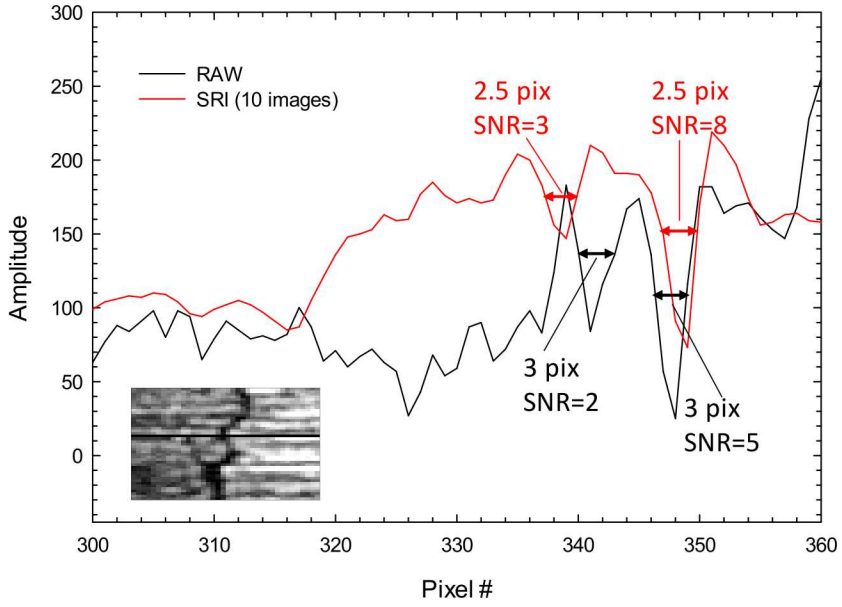

Figure 28. Plot of improvement in SNR due to the SRI processing for the GE camera. Black is single image and red is SRI image using 10 samples. The inset image is the crack that was analyzed and shows two cracks crossed by the horizontal black line.

4.3.4. Comparison of Different Sample Sets

The final test of the SRI improvement was done by using the Dino-Lite camera to image a formal resolution target (U. S. Airforce 1963A) and to compare the signal improvement between samples of 10, 20, and 30 images. This is shown in Figure 29. The target imaged is a U. S. Airforce 1963A resolution target and the cell area 14 has 71µm pitch. Image (a) is the 71 µm pitch section of the target with a horizonal line indicating the cross-cut line. Image (b) is a magnified image of the pattern, and image (c) is the value of the cross-cut for a 10 image SRI (black), 20 image SRI (red), and 30 image SRI (green). As illustrated in image (c) of Figure 28, the amplitude of the variation from the light to dark areas of the target gets larger as we sample from 10 to 30 images and recombine them, illustrating the increase in SNR for the sample as larger numbers of images are combined. This is a very good illustration of the veracity of the technique as a single image of the target is easily viewed alone due to the precision nature of the target, yet improvement in the SNR of the image as a result of SRI processing is clearly observed even in a very high fidelity initial image.

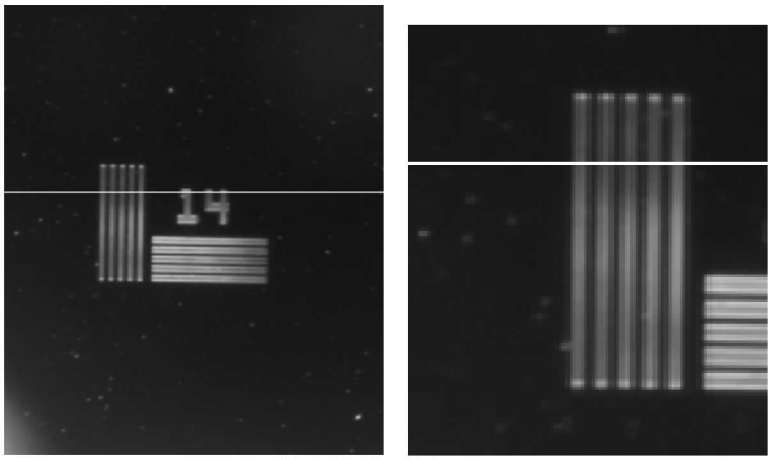

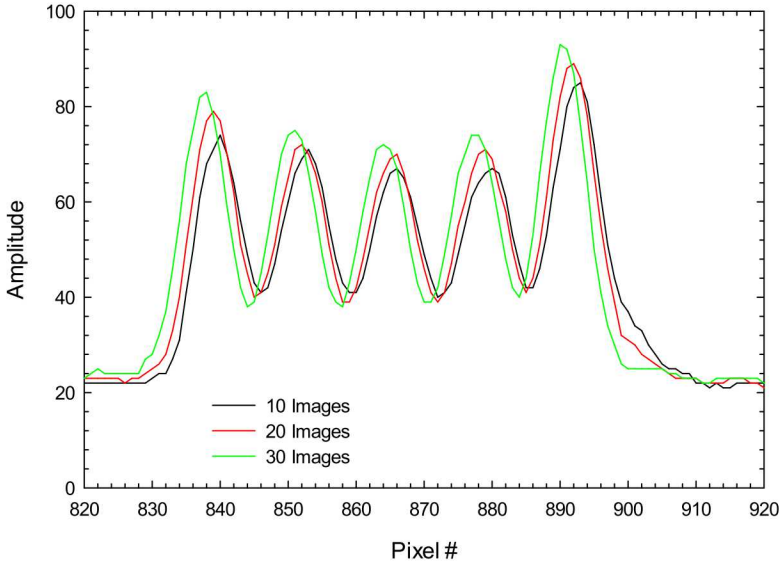

Figure 29. Comparison of SRI images of a resolution target made from 10, 20, and 30 images. Target is a U. S. Airforce 1963A resolution target. Image (a) is the 71 μm pitch section of the target with a horizonal line indicating the cross-cut line; image (b) is a magnified image of the pattern. Image (c) is a comparison of amplitudes along the cross-cut line for a 10 image SRI (black), 20 image SRI (red), and 30 image SRI (green).

5. ROBOTICS

5.1. Goals and Requirements

The novel concept for super resolution imaging requires moving an imager in small, precise increments relative to a feature of interest. Image frames are acquired at each position and combined to develop a combined image with improved resolution. Our approach depends critically on knowing the relative motion of the imager between each of the image frames in order to accurately register the individual images and produce an optimal final image. This requires extremely accurate measurement of the changes in imager position. The goal of the robotic system developed in this work was to provide this motion and measurement capability within the confined annulus between the cylinder outer surface and the overpack. As existing mobile robots exist that have been developed specifically for accessing this space, it was assumed that delivery to the site of interest would be provided by an existing system. Thus, the novel system was intended to provide fine motion and measurement, well beyond the resolution of the existing host vehicles. As super resolution imaging is a new concept for this application, the precise motion requirements for the imager were unknown. Requirements were derived primarily from the size of features to be detected, approximately 10-30 μm. Thus, motion solutions were sought that would provide incremental motion on the order of 10 μm or less, and position measurement accuracy of less than 5 μm.

The optimal type of motion of the imager was also undefined. Several options were considered, including imager translation parallel to the surface, imager rotation, and movement in an arc about a fixed point of interest (Figure 30). In order to provide flexibility, two-dimensional motion in a plane parallel to the imaging plane was selected. This would provide the ability to recreate many potential motions of interest (e.g., linear movement normal to crack direction, regardless of crack orientation) via software.

Range of motion requirements were somewhat flexible and driven primarily by the physical constraints of the confined imaging environment and the host vehicle. The total motion required to create a single SR image is well below 1 inch. However, a larger imaging region would enable multiple areas to be imaged without relocating the host vehicle. Thus the team sought to maximize the range of motion while accommodating the constraints imposed by the environment and the host vehicle.

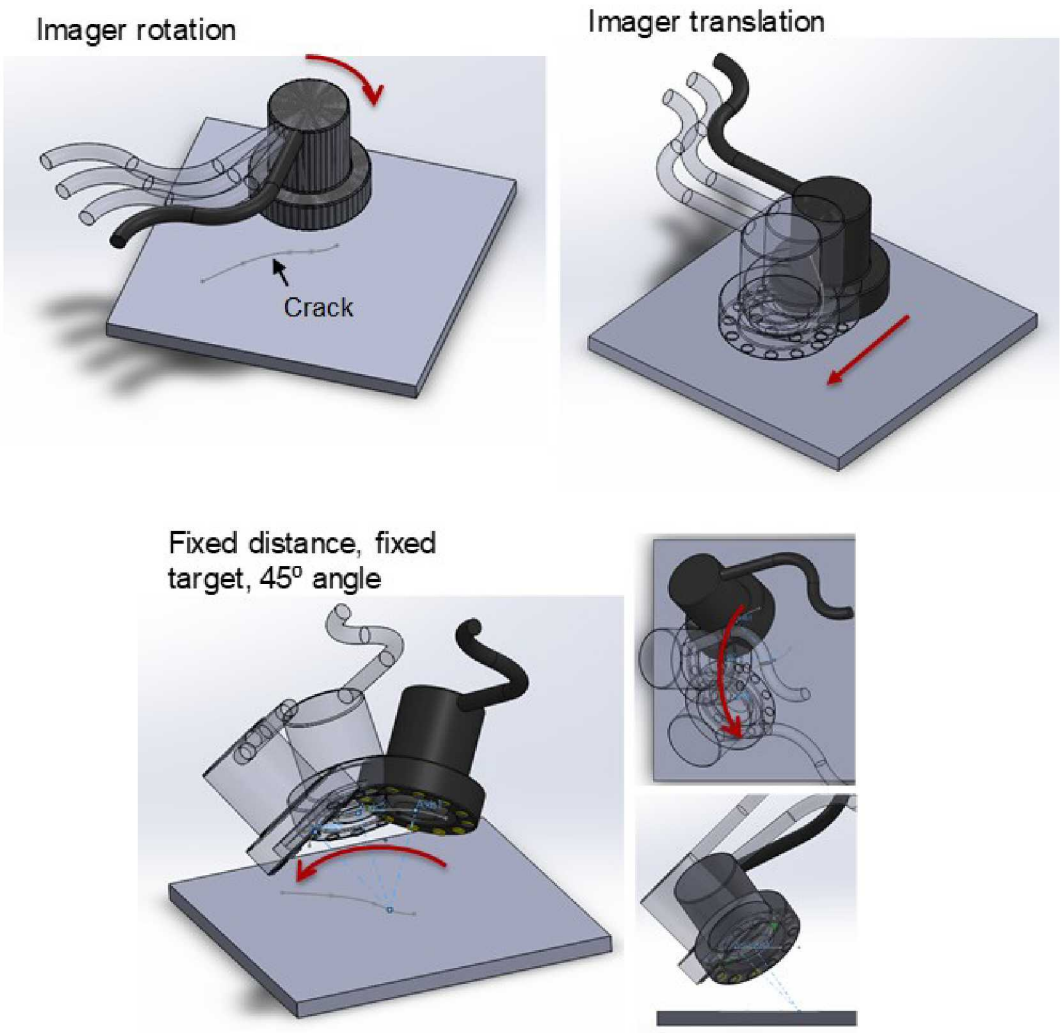

Figure 30. Example Imager Motions

The motion system was conceptualized as a modular stage that could be mounted to a host robot or delivered to the confined imaging annulus by other means. Without knowledge of the details of the host vehicle, initial concepts included elements that could independently lock the precision motion stage in place within the annulus, such that any motion of the host vehicle would not corrupt the measurement of relative position between image frames. With this capability, the module would stay fixed and the imager position could be determined entirely from position measurements internal to the module. Ultimately, the host vehicle selected was able to hold its position very well, thanks to its very strong permanent magnet wheels. Thus this requirement was determined to be unnecessary.

A final requirement was to be compatible with a moderate radiation environment. Thus concepts were favored that would not fundamentally require components that are

highly susceptible to radiation, or that would enable such components to be located outside the overpack, shielded from the canister surface.

5.2. Initial Concepts

A number of concepts were generated that explored alternative ways to meet the requirements. An initial concept is shown in Figure 31. It uses a four-bar linkage to provide a complex, though fixed, trajectory for an imager to move in a prescribed arc around a desired imaging target. This concept used a high-reduction worm gear to provide very finely controlled endpoint motion with a conventional DC motor as an actuator. Contained within each of four corner structures is a mechanism that would allow stanchions to extend to brace the module within the annulus. This mechanism could include a central cam that would extend the stanchions when rotated, and a pair of cables (e.g. integrated in a borescope structure) that would effect rotation of the cams. Figure 32 shows how such a module could integrate conceptually with an existing robotic platform to access the annulus. It also shows the stanchions extended to apply pressure to the annulus surfaces to brace the module in place. The primary drawback of this design is the fact that the motion of the imager is permanently encoded in hardware, and cannot be easily changed.

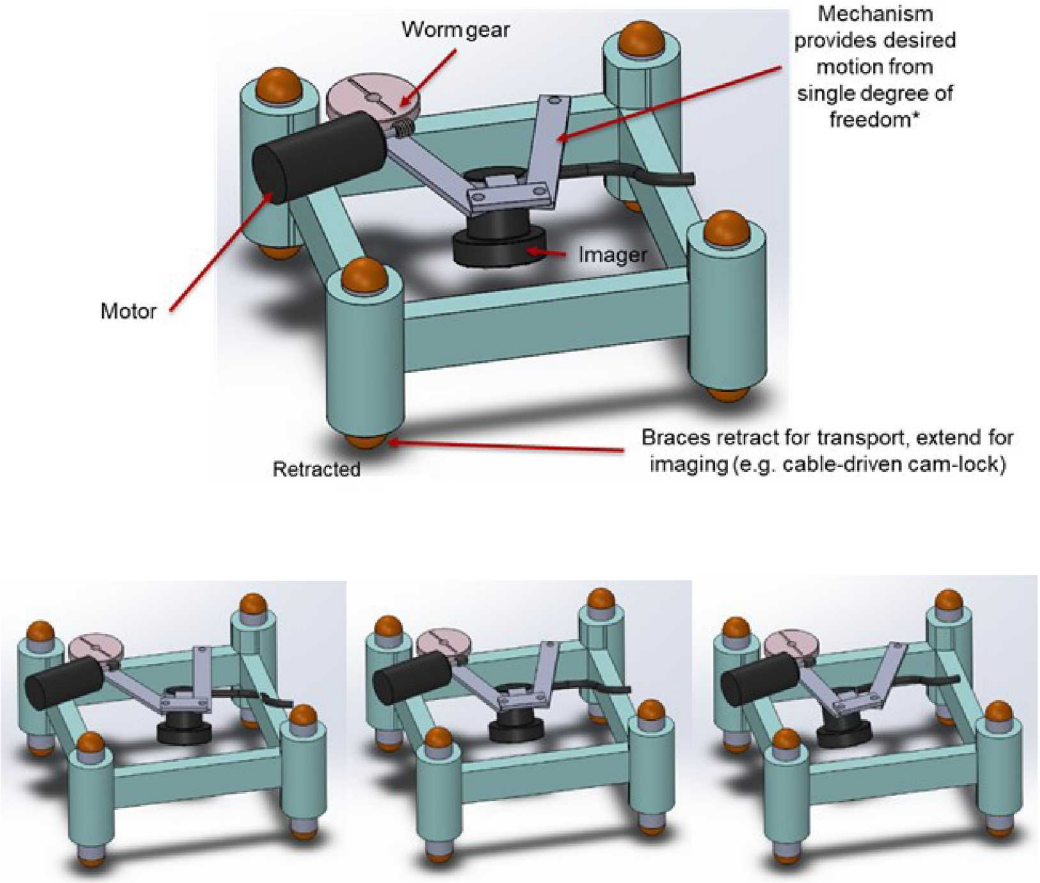

Figure 31. Early concept for imaging system, using a 4-bar linkage to control camera motions.

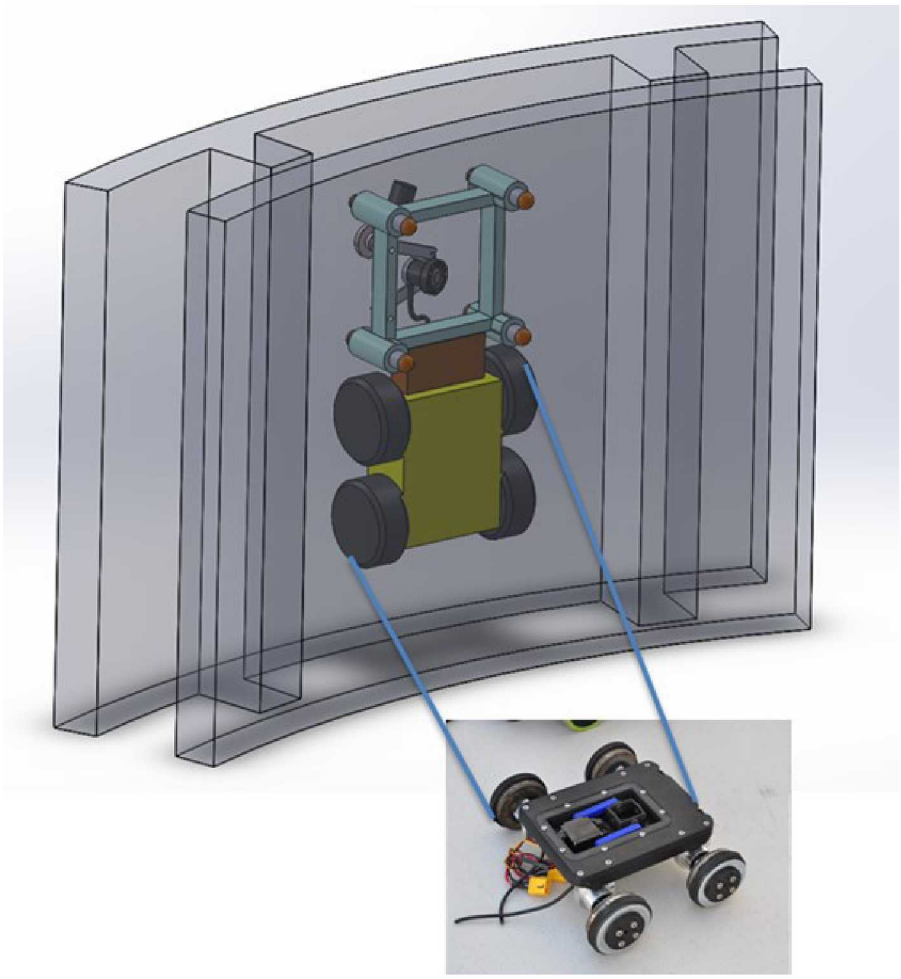

Figure 32. Views of initial concept, deployed within the annulus of a storage system.

An additional concept is shown in Figure 33. This concept was designed to integrate with a specific robot from Penn State University, and mimics its multi-wheel structure. The Penn State robot includes a "train" of several modules, and this module was designed to be another element in this train. Unlike the other modules, this design includes an ability to brace the module within the annulus by extending some of the wheels away from the main driving surface when actuated. Figure 34 shows this mechanism working, and shows how the unit would fit in the annulus. This design includes planar "XY" motion in a plane parallel to the surface to be imaged, enabling programmable motion of the imager.

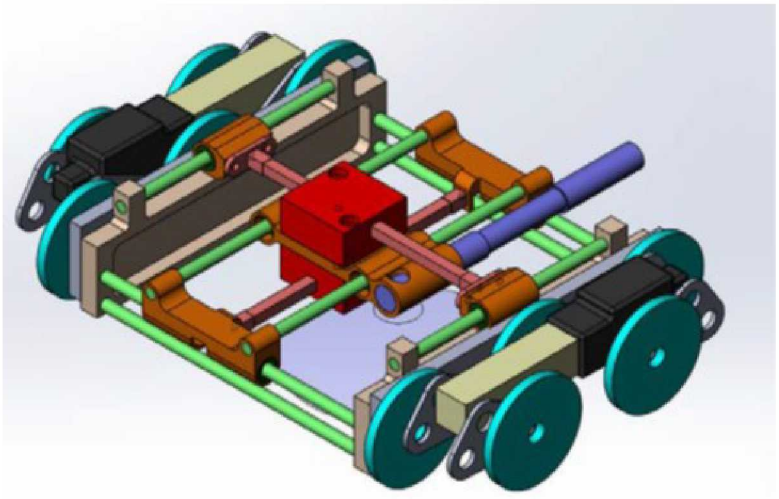

Figure 33. Preliminary concept, designed to work with Penn State robotic "train".

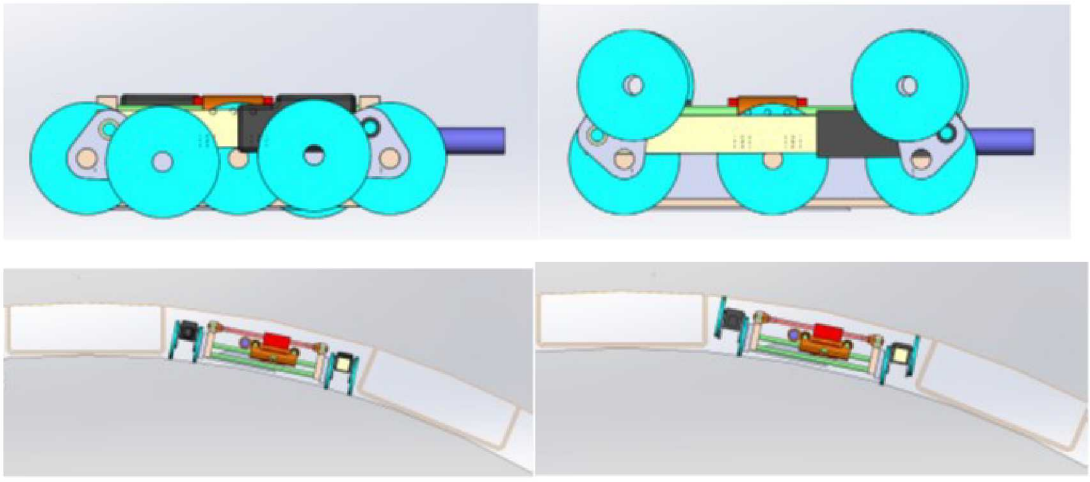

Figure 34. Train concept included bracing wheels, to lock the instrument in place within the annulus.

Several other design configurations were considered before settling on the final design described below.

5.3. Final Design

A prototype of the final module design is shown in Figure 35. The prototype is designed to precisely move a GE XLG3T84120SN imaging tip, attached to a GE Inspection Technologies XLG3 Videoprobe, the borescope that has been used in all canister inspections to date. This imager, shown in Figure 36, uses a side-view tip with a 120° field of view and a focal length of 4-200 mm. The tip has a diameter of 8.4 mm. For many imaging applications, the tip is manipulated through an integrated borescope. This motion is not useful for the SR imaging concept because there is no ability to measure the position / relative motion of the imager with the accuracy required. Thus this motion is not used for this application. Instead, the titanium tip of the imager is tightly clamped within the module, the cable is loosely constrained, and the steering mechanism is partially back-driven. GE provided the $70K videoprobe on loan, for integration and testing with the system.

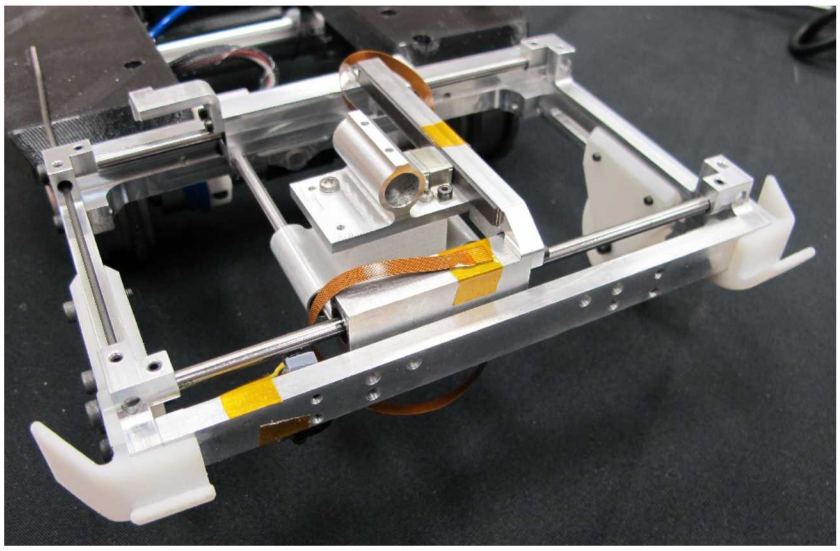

Figure 35. Completed prototype of the final module design.

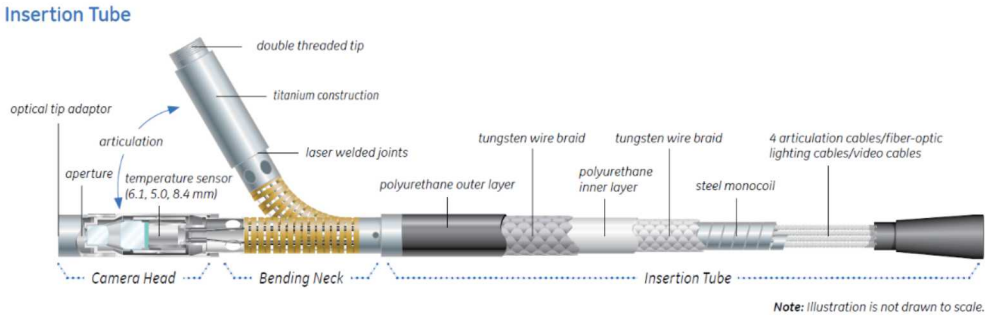

Figure 36. GE XLG3T84120SN imaging tip, used with a GE Inspection Technologies XLG3 Videoprobe

The module was designed to integrate with an existing robotic delivery system from Robotic Technologies of Tennessee (RTT) (Figure 4). This robot has been used in several demonstration projects, illustrating its ability to penetrate and explore NAC-type vertical storage systems; one was purchased for integration and testing of the imaging system. The robot is shown traversing a mockup ventilation outlet for a NAC storage system in Figure 37 A rendered solid model of the robot is shown in Figure 38. The robot contains permanent magnets in its wheels that provide adhesion to the steel overpack surface. Four brush motors drive the wheels; however, the motors on each side are electrically tied together to provide identical motion. The vehicle can drive forward and back and steer via differential rotation. The robot typically includes a camera and light bar at the front to facilitate driving, as well as a lighted camera in the rear. It has a central bay to accommodate payloads. However, if our motion stage was confined to this space, it would not be able to image significant areas of the cylinder exterior since the robot motion is limited by the structural ribs in the annulus. Instead, we sought to be able to image as close to the sides of the robot as possible. Thus we elected to add our module to the front of the robot.

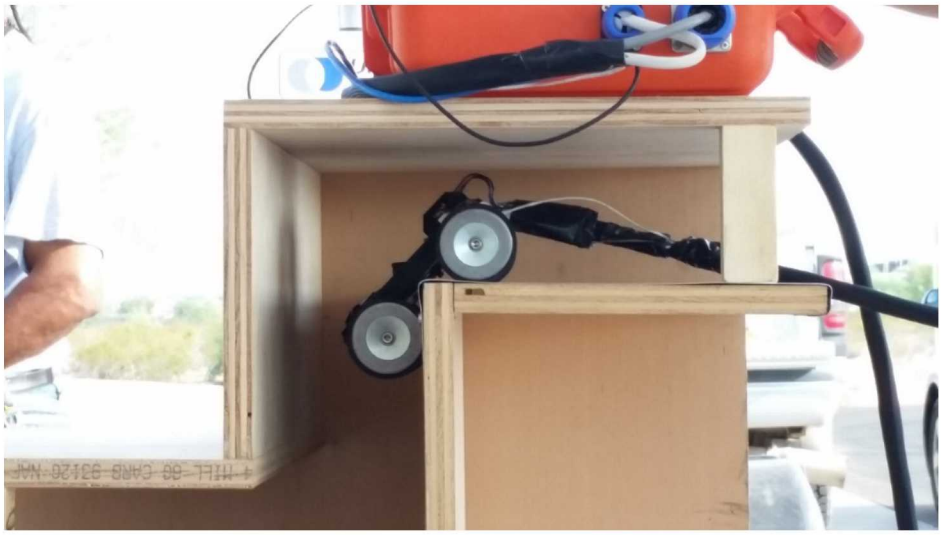

Figure 37. Magnetic Wheeled RTT robot traversing a mockup of a SNF dry storage system outlet vent.

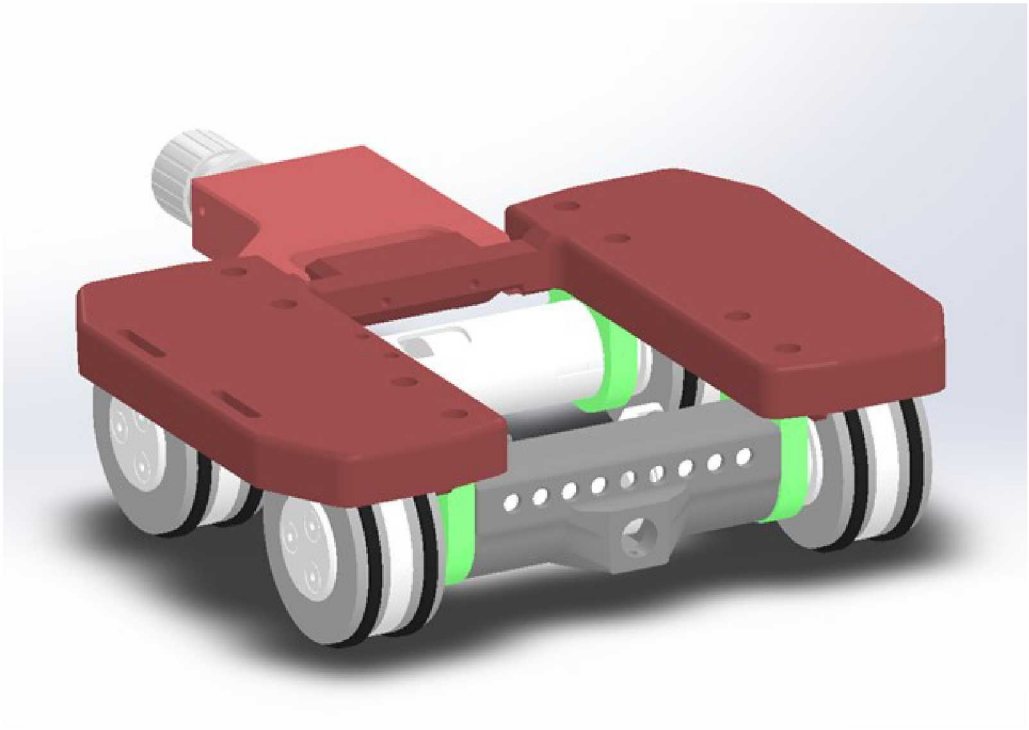

Figure 38. Rendered solid model of the RTT robot.

5.4. Motion Module

A model of the motion module is shown in Figure 39. The module provides approximately 3.8 inches of total travel in the direction orthogonal to robot travel, and approximately 2.0 inches of travel in the direction of robot travel. The module includes two passive wheels that hold it in the desired location relative to the driving surface. The imager is represented by the blue rod visible at the top of the module, and the cone shows its field of view. The robot and module ride on the surface of the overpack, therefore the surface of the cylinder is imaged by looking "up" to the surface opposite that on which the wheels ride.

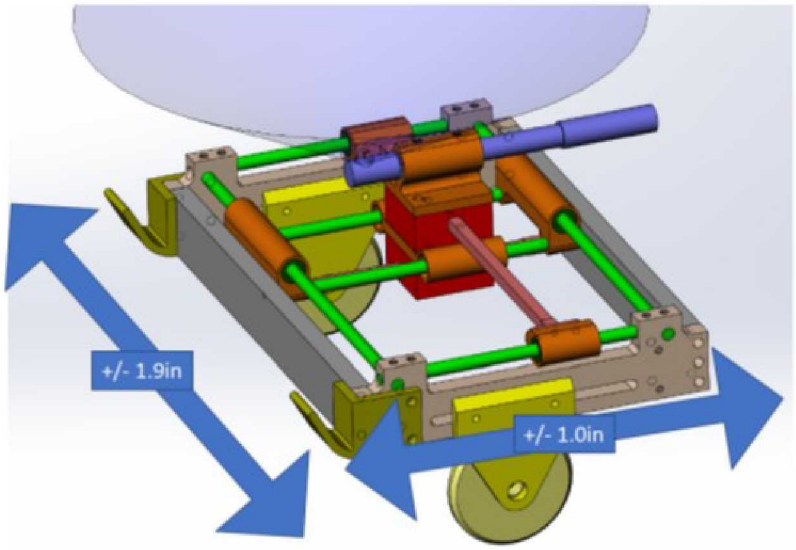

Figure 39. Rendered model of the camera motion module.

Precision motion is accomplished via stepping piezo linear actuators from PI, shown in Figure 40. These actuators can achieve a resolution of 1 nm open loop – far better than required – but can still move at the relatively high speed of 10 mm/sec. They can generate 10 N of force, much more than required to move the imager. The design includes RoLin miniature packaged incremental magnetic encoders from RLS, also shown in Figure 40. These achieve a specified measurement accuracy of 1μm. Since the actuators can provide finer resolution than we are able to measure with the encoders, we did not intend to close a control loop around the encoders. Similarly, if the PI actuators are able to complete their steps as commanded, the open-loop position is far more precise than what can be measured with the RLS encoders. Therefore, the encoders are used simply as a check to ensure that the actuators have reached their desired positions, while the camera location for SR imaging purposes is to be determined by the commanded actuator steps.

Figure 40. Motion control is accomplished via PI Piezo linear actuators (left), and RLS incremental magnetic encoders (right).

Unfortunately, unexpected supply issues at the piezoelectric actuator provider forced us to adapt our design to include different actuators in attempt to ensure a complete functioning system in time for planned integration. We acquired low-cost DC-motor-driven actuators and packaged them using 3D printed mounts as a drop-in replacement for the high-precision piezo actuators. While these actuators are unable to provide precise positioning, since the high-resolution encoders are still present we are able to determine the location of the imager with sufficient accuracy to enable effective registration for SR image processing. The inclusion of the modified actuators reduces the available travel to 50 mm total travel normal to robot motion, and 20 mm total travel in the direction of robot motion – still sufficient to image stress corrosion cracks. The revised model, including these actuators, is shown in Figure 41.

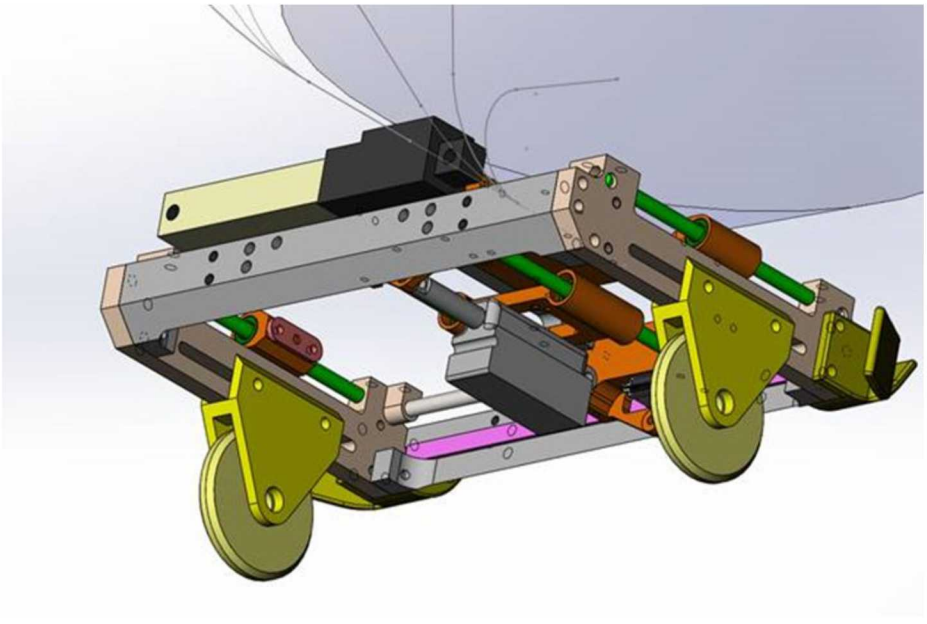

Figure 41. Rendered model of the prototype imager, with the substitute actuators in place.

5.5. Combination with robot

With the module significantly extending the overall length of the robotic delivery system, it is important to ensure that the module does not impede the robot's ability to navigate the ventilation channel into the annulus. Therefore the module connects to the robot with a pin joint that enables motion of almost 90 degrees in each direction. The module rotates around the front axle of the vehicle and includes passive wheels that allow it to ride on the surface in front of the robot. The module pivot around the axle is spring-loaded to keep the wheels in contact with the driving surface. The module includes fingers extending from its front that cause the module to pivot up when the robot drives it into a vertical surface, ensuring passage through the access channel. A series of model snapshots are shown in Figure 42, showing that this configuration is designed to be able to traverse the ventilation channel.

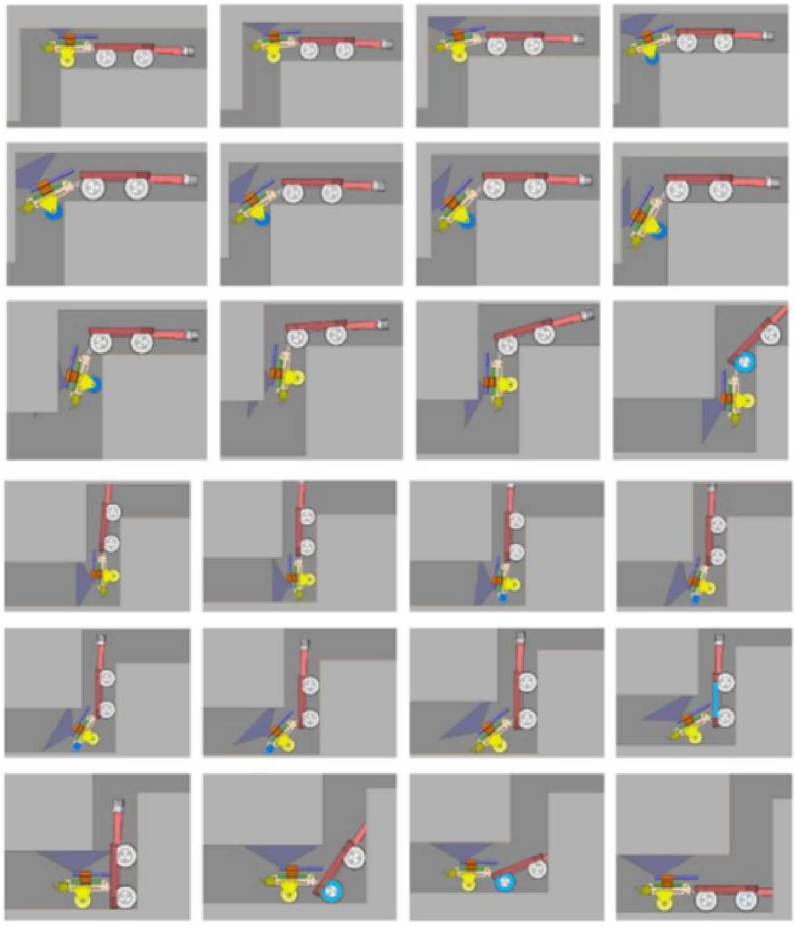

Figure 42. Rendered model of the robot and imaging module traversing right-angle bends in the ventilation channel for a NAC storage system.

5.6. Prototyping and Fabrication

The motion module was prototyped using a combination of machined aluminum and 3D printed nylon parts. Control software was developed to enable the use of each different type of actuator (precision PI actuators and low-cost DC actuators) as well as the encoders. A screenshot of a code snippet and a prototype graphical user interface are shown in Figure 43.

Two photographs of the module integrated with the robot are shown in Figure 44. The module obscures the camera and light emitting diode (LED) light bar that are typically mounted on the robot's front axle. A replacement camera and light bar were acquired for mounting on the front "bumper" of the module to support driving (not shown).

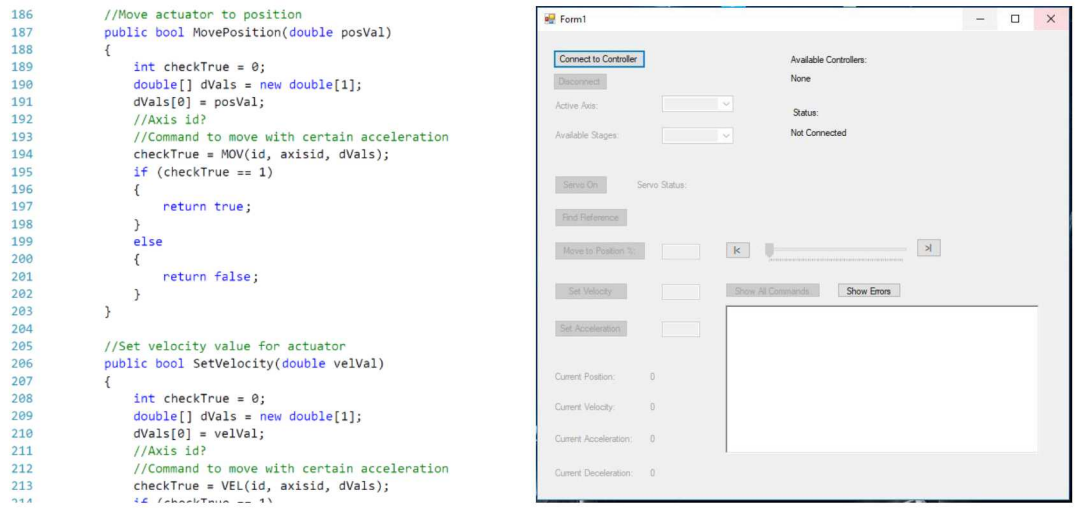

Figure 43. Code snippet and screenshot of prototype graphical user interface from stage control software.

Figure 44. Photographs of the integrated imaging module and magnetic robot.

5.7. Test frame

A mockup was constructed to emulate the ventilation channel geometry that the system must traverse to enter the annulus between the cylinder and overpack. This mockup is made of wood with steel sheet to enable magnetic adhesion. The channel is generally 3 7/8" across and requires two 90 degree transitions both "downward" and "upward" relative to the robot. The mockup is shown in Figure 45.

The mockup was used to test the ability of the combined robot/imaging module system to traverse the ventilation channel and to enter the annulus. Within the annulus, SCC test samples can be mounted for testing the imaging module. The full system, including robot with module, controller, and mounted GE camera, is shown in Figure 46. Images of the combined system traversing the mockup and entering the annulus

are shown in Figure 47. Additional close-up images of the robot traversing the mockup are shown in Figure 48. Images of the camera in an appropriate location for imaging with respect to the mockup cylinder surface are shown in Figure 49. The camera was successfully delivered to this location using the robotic system.

Figure 45. Ventilation channel mockup used for testing the robot/imager system.

Figure 46. Images of the combined robot/imaging module traversing the storage system mockup.

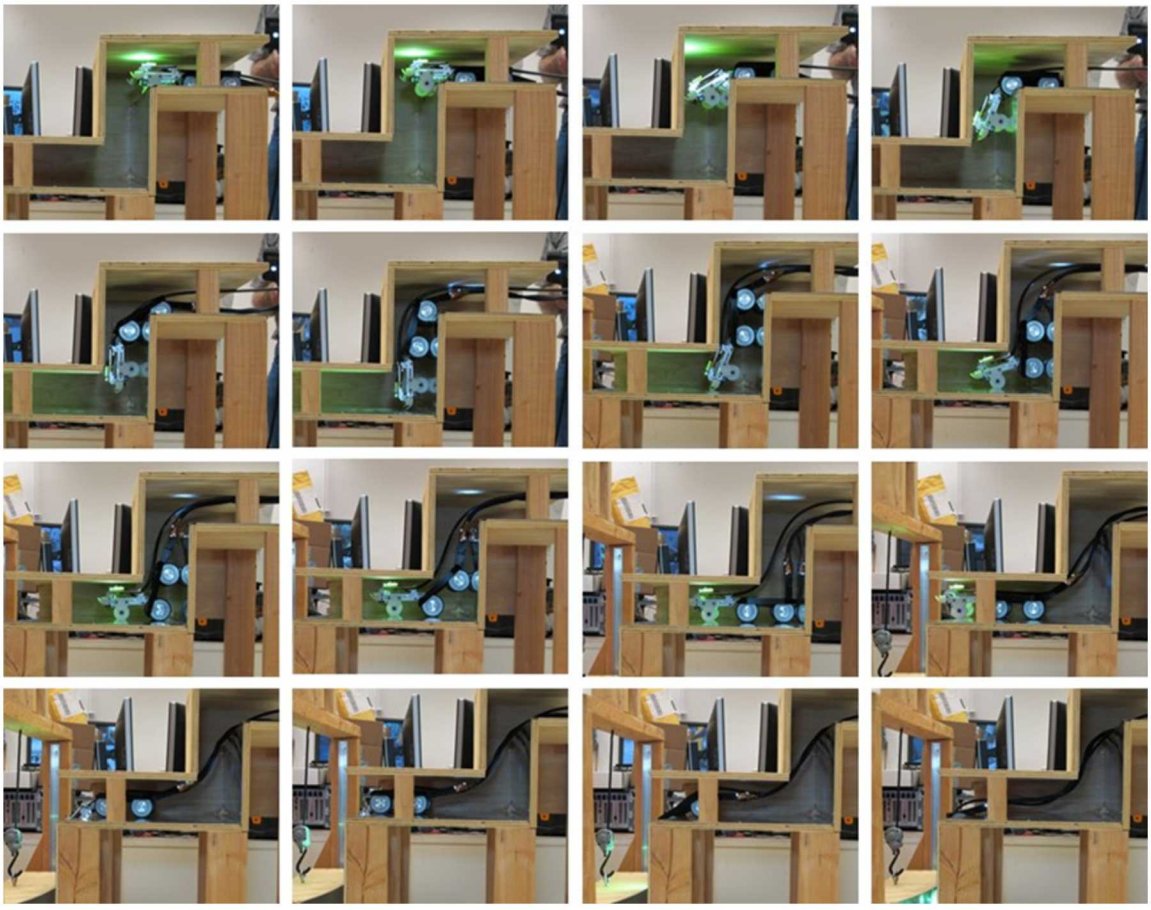

Figure 47. Sequence image of the robot and imaging module traversing the mockup. Analogous to Figure 42.

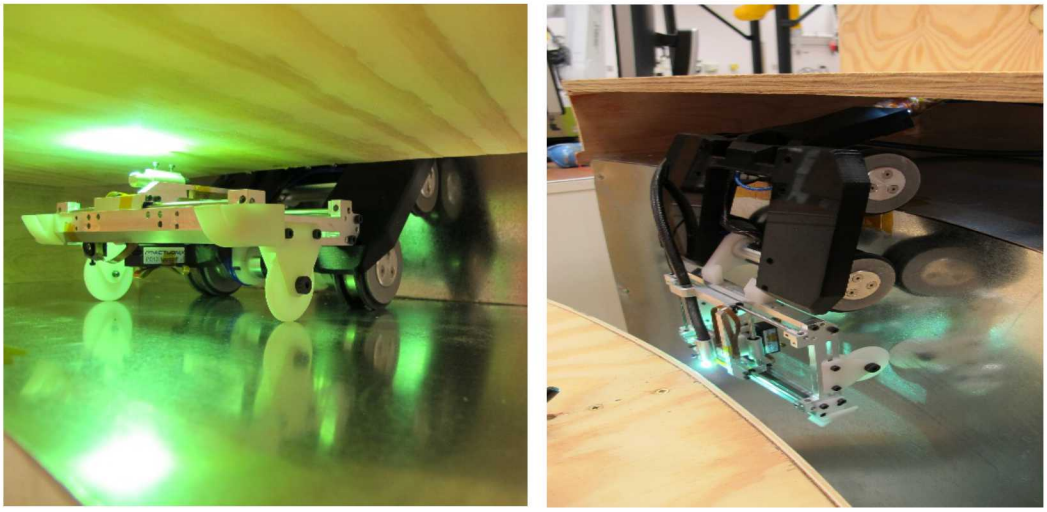

Figure 48. Close-up images of the combined robot/imaging module traversing the storage system mockup.

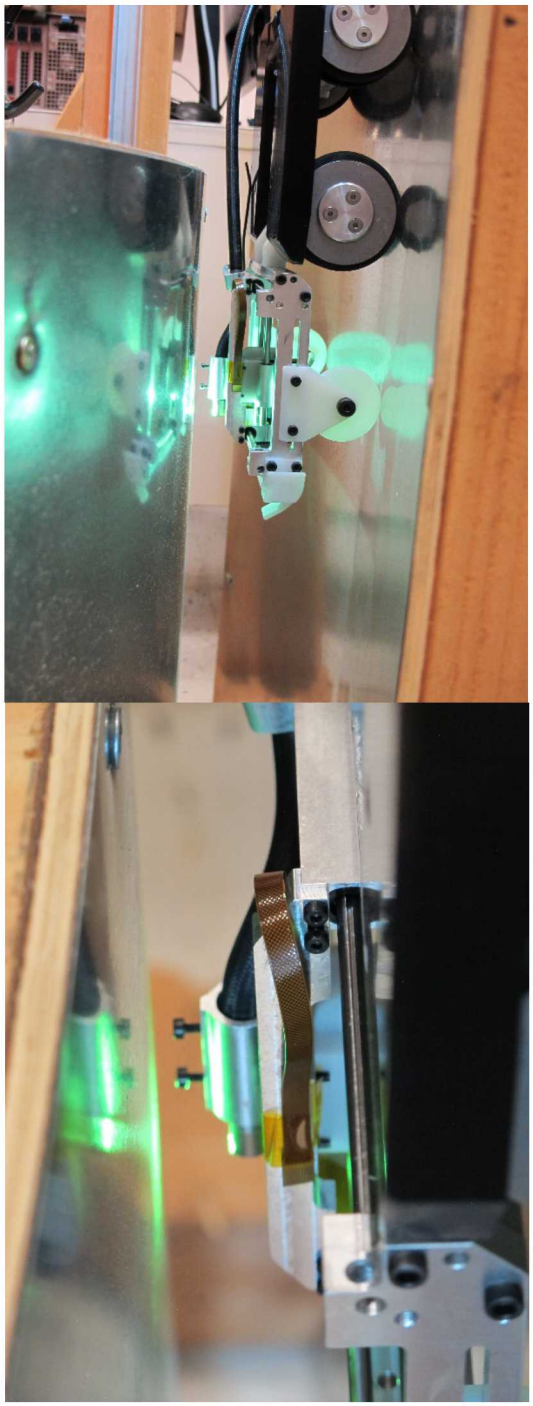

Figure 49. Images of the camera, located by the motion module and robot, imaging the mockup cylinder surface.

5.8. Performance of the Combined Robot/Camera System

At the time of this writing, all of the key system elements have been demonstrated independently or as subsystems, but a complete end-to-end experiment has not yet been conducted. End-to-end operation requires additional wiring and software integration to enable operation of the motion stage with all of the other elements *in situ*, and is expected to be complete in the near future.

The work to date serves as a successful proof-of-concept, demonstrating that an appropriate imaging system can be delivered through the available access channel to the surface of a NAC canister mockup, and that such an imaging system may be used with super-resolution imaging techniques to locate extremely small stress corrosion cracks. To mature the system to a level suitable for field use requires several additional steps including:

- The more precise PI actuators, for which the motion module was designed, must be integrated to provide greater range of motion and better imaging performance

- The software that controls the three main subsystems (motion module, magnetic robot, and imaging) must be integrated. Using the borrowed GE camera, the team was not able to find any way to electronically trigger imaging to synchronize it with the stage's steps. This would currently require a highly manual process that would be impractical for field use. Ideally all three subsystems would be controlled through a single interface, and acquired images could be natively and automatically tagged with camera location as they are stored. GE is currently working on the next-generation imager, which may be more flexible with respect to external control.

- Packaging and cabling for the robot, motion module and imager should be re-engineered to improve cable management and robustness. An iteration of the custom hardware, plus cooperation with the robot and imager vendors, would be required to produce a robust field system.

- In order to be used for an *in situ* inspection, SR image processing and analysis would have to be carried out real-time, allowing further inspection of potential indications. This requires that the software be automated, to produce SR images immediately upon image collection.

6. CONCLUSIONS

Stress corrosion cracks represent a major concern for the structural integrity of engineered metal structures, and standard visual techniques for detecting SCC, frequently used in difficult-to-access environments, are ineffective. Here, we have created and tested an improved optical sensor for SCC in restricted access-environments by combining optimized, controlled camera movements and super-resolution image processing. SRI processing combines multiple images of a subject to create a final image that has a higher resolution than any of the individual images used to create it. Our method improves the likelihood of detecting SCC, and potentially revolutionizes techniques for remote visual inspections of any type. Our approach is innovative in that we utilize *a priori* knowledge of the camera location for each individual image to align, or register, the images with each other, resulting in a superior SRI final image relative to techniques using software registration.

To evaluate this approach, benchtop testing was performed with three different cameras; a laboratory digital microscope, a coarsely pixelated coherent fiber optic borescope, and a high resolution CCD-based borescope used in industry visual inspections. High-precision X-Y and rotational stages were used in these tests, along with laboratory-created test samples with real SCC cracks. Testing indicated that SRI processing improved crack imaging with all imaging devices. Moreover, testing indicated that pre-processing to remove lens distortion was effective in improving final images; for the fiber optic borescope, additional pre-processing with a fast Fourier transform filter to remove coarse optical fiber pixelation was also useful. Testing also showed that final image quality improved with the number of images combined. Finally, the benchtop tests confirmed that using *a priori* knowledge of the camera location for each individual image resulted in a higher quality combined image.

Having confirmed the benefit of using the camera location to register the individual images, we designed and built a high-precision module for controlling camera motions. This system was built for the specific application of inspecting spent nuclear fuel storage canisters within their overpacks. Access to the canisters is limited by narrow ventilation channels through the overpacks and narrow annuli between the overpack and the canister surface. Moreover, high radiation levels and potentially elevated temperatures can be present. Rather than developing a robot to enter the overpack, the module was designed to be coupled to an existing robotic delivery system designed by Robotic Technologies of Tennessee. This magnetic-wheeled robot is capable of entering the overpack and the annulus by traveling on the carbon steel wall of the overpack. The system also incorporated a high-resolution videoprobe borrowed from GE Inspection Technologies, that has been used in several canister inspections to date.

To test the combined robot/camera module system, a wood and steel mockup of a NAC International SNF storage system was built, including the steel-lined ventilation channel through the overpack, and a portion of the annulus between the canister and

the overpack. The system was designed so that a SCC test sample could be mounted to the “canister” for testing purposes. The combined robot/imager system successfully

navigated the tight ventilation channel and entered the annulus, positioning itself to inspect the canister surface. This demonstrates that the system could be used in a real storage system.

This work serves as a successful proof-of-concept, demonstrating that an appropriate imaging system can be delivered through the available access channel to the surface of a NAC canister mockup, and that such an imaging system may be used with SR imaging techniques to locate extremely small stress corrosion cracks. All of the key system elements have been demonstrated independently or as subsystems, but a complete end-to-end experiment has not yet been conducted. To mature the system to a level suitable for field use requires several additional steps, including software development for controlling the motion module and for integration with the imager; re-engineering packaging and cabling for the robot/image system to improve cable management and robustness; and software automation for real-time SRI processing and analysis. With additional effort the imaging system built here could be the basis for a robust SCC crack detection system for deployment in spent nuclear fuel storage systems.

REFERENCES

1. Wåle, J., *Crack Characterization for In-Service Inspection Planning – an Update*. Swedish Nuclear Power Inspectorate: Stockholm, Sweden, 2006
2. Cumblidge, S., M. Anderson, and S. Doctor, *An assessment of visual testing*. Pacific Northwest National Lab, Richland, WA, 2004.
3. Satoh, Y., J. Suzuki, and T. Ootsubo, *Advanced Visual Testing Technologies for In-Vessel Inspection.* Presentation EJAMOT10 2010.
4. Tian, J. and K.-K. Ma, A survey on super-resolution imaging. *Signal, Image and Video Processing* 5(3): p. 329-342, 2011.
5. Farsiu, S., et al., Advances and challenges in super-resolution. *International Journal of Imaging Systems and Technology* 14(2): p. 47-57, 2004.
6. Rangarajan, P., et al., Active computational imaging for circumventing resolution limits at macroscopic scales. *Applied Optics* 56(9): p. D84-D107, 2017.
7. Israel, Y., et al., Quantum correlation enhanced super-resolution localization microscopy enabled by a fibre bundle camera. *Nature Communications* 8: p. 14786, 2017.
8. Liang, H., et al., The NAMlet transform: A novel image sparse representation method based on non-symmetry and anti-packing model. *Signal Processing* 137: p. 251-263, 2017.
9. Kato, T., H. Hino, and N. Murata, Double sparsity for multi-frame super resolution. *Neurocomputing* 240: p. 115-126, 2017.
10. Wang, H., et al., Fast single image super-resolution using sparse Gaussian process regression. *Signal Processing* 134: p. 52-62, 2017.
11. Kain, R.M., Marine atmosphere corrosion cracking of austenic stainless steels. *Materials Performance* 29(12): p. 60-62, 1990.
12. NWTRB, *Evaluation of the Technical Basis for Extended Dry Storage and Transportation of Used Nuclear Fuel.* NWTRB. p. 145, 2010.
13. EPRI, *Extended Storage Collaboration Program (ESCP) Progress Report and Review of Gap Analyses*. Palo Alto, CA. p. 234, 2011.
14. Hanson, B., et al., *Gap analysis to support extended storage of used nuclear fuel.* U.S. Department of Energy. p. 218, 2012.
15. NRC, *Potential Chloride Induced Stress Corrosion Cracking of Austenitic Stainless Steel and Maintenance of Dry Cask Storage System Canisters*. U.S. NRC: Washington, D.C., 2012.
16. Palmer, J.M. and B.G. Grant, *The Art of Radiometry*. Bellingham, Washington: SPIE Press, 2010.
17. Batinga, D. *What is the Resolution of the Human Eye?* Available from: https://futurism.com/what-is-the-resolution-of-the-human-eye/, 2016.

18. Clark, R.N. *Notes on the Resolution and Other Details of the Human Eye*. Available from: http://www.clarkvision.com/articles/eye-resolution.html, 2017.

19. IStillShootFilm. *The Real Resolution of Film vs. Digital*. Available from: http://istillshootfilm.org/post/114131916747/the-real-resolution-of-film-vs-digital, 2015.

20. Sze, S.M., *Semiconductor Devices: Physics and Technology, 2nd Edition*. Hoboken, NJ: John Wiley and Sons, Inc. 213 p., 2002.

21. Knoll, G., *Radiation Detection and Measurement. 3rd Edition*. New York, NY: John Wiley and Sons, Inc, 2000.

22. Neo, A., et al., Investigation of super-resolution processing algorithm by target light-intensity search in digital holography. *Optics Communications* 389: p. 85-91, 2017.

23. Hecht, E. and A. Zajac, *Optics. 2nd Edition*, Menlo Park, CA: Addison-Wesley Publishing Co. 768 p., 1974.

24. Wilson, M., *Microscope Resolution: Concepts, Factors and Calculation: Airy Discs, Abbe's Diffraction Limit and the Rayleigh Criterion.* Available from: https://www.leica-microsystems.com/science-lab/microscope-resolution-concepts-factors-and-calculation/, 2016.

25. Mathworks. *Single Camera Calibrator App*. Available from: http://www.mathworks.com/help/vision/ug/single-camera-calibrator-app.html, 2018.

26. Rorabaugh, C.B., *DSP Primer*. New York, NY: McGraw-Hill, 2008.

27. Enos, D. and C. Bryan, *Final Report: Characterization of Canister Mockup Weld Residual Stresses*. U.S. DOE. 62 p., 2016.

28. Mathworks, *MATLAB Version R2018a*, Nantick, MA.

29. Adams, M.J., *An Introduction to Optical Waveguides*. Chichester: John Wiley and Sons, Inc., 1981.

30. Dickey, C., *Irradiation of fiber optics in the SSC tunnel*. Superconducting Super Collider Lab. 16 p., 1990.

31. Berghmans, F., et al. Radiation hardness of fiber optic sensors for monitoring and remote handling applications in nuclear environments. In *Process Monitoring with Optical Fibers and Harsh Environment Sensors*. International Society for Optics and Photonics, 1999.

DISTRIBUTION

1 Ned Larson (electronic copy)
M/S NSF 165, Room B119
U.S. Department of Energy
232 Energy Way
North Las Vegas, NV 89030 (Ned.Larson@doe.gov)

1 Jeremy Renshaw (electronic copy)
Program Manager, Used Fuel and High Level Waste
Electric Power Research Institute
1300 West WT Harris Blvd.
Charlotte, NC 28262 (jrenshaw@epri.com)

1 Jim Stadler (electronic copy)
AIS Growth Leader
GE Inspection Technologies
1002 Geneva Street, Unit B
Shorewood IL 60404 (jim.stadler@bhge.com)

1 Steve Glovsky (electronic copy)
Executive Vice President
Robotic Technologies of Tennessee
2560 Nova Circle
Cookville, TN 38501 (sglovsky@robotictechtn.com)

1	MS1425	Stephen A. Casalnuovo	8630
1	MS1425	Ronald P. Manginell	8634
1	MS1425	Kent B. Pfeifer	8634
1	MS0899	Technical Library	9536 (electronic copy)
1	MS0359	D. Chavez, LDRD Office	1911

Sandia National Laboratories